THE CHARACTERIZATION OF AN ATMOSPHERIC OPTICS FACILITY

A Thesis

by

GRANT EARL ERICKSON

Submitted to the Graduate and Professional School of
Texas A&M University
in partial fulfillment of the requirements for the degree of

MASTER OF SCIENCE

Chair of Committee,	Christopher Limbach
Committee Members,	Richard Miles
	Waruna Kulatilaka
	Diego Donzis
Head of Department,	Ivett Leyva

May 2022

Major Subject: Aerospace Engineering

ABSTRACT

The Atmospheric Optics community currently relies on theoretical approximations of both turbulence characteristics and beam perturbations for the design and analysis of emerging technologies such as directed energy and optical communication links. In order to quantify the applicability and accuracy of such models it is advantageous to study beam propagation within a controlled aerodynamic environment. While several such facilities have been used in the past, direct measurement of parameters such as the refractive index structure constant and turbulent length scales have been lacking and can lead to over-reliance on theoretical assumptions. This work reports on controlled beam propagation experiments in Texas A&M's Subscale Atmospheric Facility (SAF) wherein scintillation, Filtered Rayleigh Scattering (FRS), and parallel beam correlation experiments were conducted to quantify turbulence parameters and Atmospheric Optic effects without conventional reliance on theoretical assumptions. Key findings include the scaling of the scintillation index as L^3 over a wide ranging of turbulence strength where the inner scale ranged from $5.2mm < l_o < 7.8mm$ as measured by two-beam correlation experiments. Furthermore, the refractive index structure parameter C_n^2 varied from 2.93×10^{-11} to 1.01×10^{-10} $\mathrm{m}^{-2/3}$ dependent on the heat dissipation rate of the wire turbulence generator.

DEDICATION

This dissertation is dedicated to Lueron and Earl Erickson.

ACKNOWLEDGMENTS

This thesis work is the culmination of a year and a half's research at Texas AM's LDPDL, but I have been a part of Texas AM's Aerospace Engineering department for the past 4 and a half years. In that time I have been fortunate to have learned from many many great mentors and peers.

I would like to start off thanking my advisor Dr. Chris Limbach. Before he was my advisor, he was my favorite lecturer. I want to thank you for the amount of knowledge, time, and wisdom you have poured into me over the past 5 years. The opportunity to work under your direction was a pivotal point in my academic career. I would not be where I am today without your guidance and for that I am forever grateful.

I would like to acknowledge and thank my advisory committee members, Dr. Waruna Kulatilaka, Dr. Richard Miles, and Dr. Diego Donzis. Their help in writing my final thesis was very much appreciated.

Next I would like to thank the whole ALLEMO team. Thank you Mr. Kochan for the construction lessons. Thank you Dr. James Creel for the many answers to my questions and the help with anything I needed. Furthermore, I would like to thank my fellow graduate students Frisco Koelling, Maddie Hetlage, Boris Leonov, Hayden Morgan, and Clark Peterson. Thank you all tremendously, it truly does take a village in research and I have been fortunate to have a great village the past year and a half.

I would also like to thank Drs. Richard Miles, Diego Donzis, Komal Kumari, and Albina Tropina for everything I learned from our countless Atmospheric Optics meetings. I am grateful for having the opportunity to be in such close contact with great minds as you all.

I would also like to thank Dr. Moble Benedict and the research team in the Advanced Vertical Flight Lab. Dr. Benedict taught me how to be an engineer and sparked my aspiration for research and development.

CONTRIBUTORS AND FUNDING SOURCES

Contributors

This work was supervised by a dissertation committee consisting of Professor Christopher Limbach (committee chair), Professor Richard Miles (committee member), and Dr. Diego Donzis (committee member) from the Texas A&M University Department of Aerospace Engineering, and Professor Waruna Kulatilaka (committee member) from the Texas A&M University Department of Electrical Engineering.

A portion of the work disclosed in this thesis was done in collaboration with, or received a contribution from, the following people: Frisco Koelling, John Kochan, Professor Diego Donzis. All other work conducted for the dissertation was completed by the student independently.

Funding Sources

Research was sponsored by the Army Research Office and was accomplished under Cooperative Agreement Number W911NF-19-2-0243. The views and conclusions contained in this document are those of the authors and should not be interpreted as representing the official policies, either expressed or implied, of the Army Research Office or the U.S. Government. The U.S. Government is authorized to reproduce and distribute reprints for Government purposes notwithstanding any copyright notation herein.

NOMENCLATURE

L	propagation distance
C_n^2	refractive index structure parameter
σ_χ^2	log-amplitude variance
E	field of electromagnetic wave
n	refractive index
c	speed of light through free space
F	Fresnel number
D	lens diameter
A	amplitude of plane wave
r	radius of laser beam
σ_I^2	scintillation index
l_o	smallest scale of turbulence before dissipation occurs
L_o	distance at which 2 points in the flow become uncorellated
U	optical field amplitude
U_o	vacuum optical field amplitude
ϕ	phase perturbation
χ	log amplitude perturbation
λ	wavelength
k	wavenumber

d	initial distance between co-propagated laser beams
B_x	correlation function between x displacements
B_y	correlation function between y displacements
t	time
η	number of atoms per unit area
N	number of atoms per unit volume
q_e	charge of an electron
m_e	mass of an electron
w	frequency of radiation
w_o	resonant frequency of an electron bound to an atom
$\boldsymbol{p}$	dipole moment
ϵ	permissivity constant
P_s	power caused by scattering
γ_l	dissipation coefficient
α	polarizabiliy
Ω	solid angle
σ'_{ss}	Rayleigh scattering cross section for a spherically symmetric scatterer
I	intensity of light
p	pressure
T	temperature
ρ	density

D_n	refractive index structure function
K_{GD}	Gladstone-Dale constant
R	universal gas constant
K	cumulent
f	focal length of lens
κ	spatial frequency
$\Phi_n(\kappa)$	refractive index spectrum

TABLE OF CONTENTS

Page

LIST OF FIGURES

FIGURE Page

LIST OF TABLES

TABLE Page

1. INTRODUCTION

As a laser beam propagates through the atmosphere, the beam is distorted due to turbulence and other density variations present in the medium. This poses a major problem for applications such as directed energy [2], astronomy [1] and laser communications [3] which desire an unaberrated wavefront and beam profile after very long atmospheric propagation distances > 1 km. The propagated beam's intensity, wavefront, and pointing are all effected by turbulence and significant research efforts have been devoted to the prediction and mitigation of such adverse effects.

The foundations of our current understanding of atmospheric optics were first introduced through the seminar work of Von Karman on the structure of isotropic turbulence [4]. Tatarskii[5] and Yura[6] later applied this structure to a theoretical treatment of beam propagation and distortion using perturbuation theory. One of the key results of this theoretical framework is how beam distortions scale with propagation distance and relate to turbulence parameters, such as the inner and outer scale of the turbulence environment.

Current research in Atmospheric Optics (AO) aims to understand the deviations of the true atmosphere from these theoretical foundations. This includes, for example, corrections due to non-isotropic turbulence [7], propagation through "deep turbulence" beyond the perturbative regime [8], and nonlinear propagation of ultrafast laser pulses [9]. Recently, the utility of direct numerical simulations of turbulence were used to discover a new L^4 scaling regime for very near-field propagations [10]. The extension of theories to these new propagation regimes will be tested, ultimately, within well-controlled and characterized facilities, which is the subject of this thesis.

Starting in the late 1980s a wide range of AO facilities were built, as described in the review paper by Jumper [11]. Each facility has unique capabilities. AO facilities share the following specifications. Firstly, realistic turbulence shall be introduced to the beam. Creating realistic kolmogorov turbulence allows for a comparison of experiments to actual use cases. Next, an AO facility shall be controllable. A controllable facility can accommodate multiple experimental test cases. An AO facilty shall have reproducible characteristics. A reproducible environment enables

consistency of results between experimental sessions.

With these specifications in mind, various facilities have been built with a specific AO focus. Each facility contains unique advantages and disadvantages. For instance, outdoor ranges such as the Navy Research Lab's Chesapeake test range and the Starfire oprical range are how propagated laser's react to ground level atmospheric turbulence [12] [13]. Unfortunately, outdoor test ranges are dependent on the outdoor conditions at the time of test. The experimental conditions cannot be adjusted or reproduced, compromising the controllability and reproducibility of the test data. For example, it is reported by Mahon that the log-normal variation of intensity of a propagated beam varied from 0.3 to 2 in the hour between dawn and after sunrise sunrise over a 19km direct link in the Slate valley[14]. This drastic change is so large that it spans from the "weak" turbulence assumption to "strong" in just 60 minutes. The magnitude of this volatility in parameters is a significant concern for test planning. Furthermore, the equipment used to characterize atmospheric turbulent may rely on questionable assumptions. Outdoor facilities often use scintillometers to measure the strength and length scale of the atmospheric turbulence [11]; however the turbulent parameters are likely variable throughout the propagation distance, leading to a nonlinear averaging effect. Moreover, scintillometers rely on theoretical assumptions to calculate key parameters, such as C_n^2 and the inner scale [15]. It was shown by Vetelino's that when comparing scintillation theory and experiment, that a stable calculation of turbulent inner and outer scales is very difficult to obtain by the scintillation theory of Andrews et. al [16] [17]. The experiment conducted by Vetelino using such devices did not converging on confident values for turbulent scales.

To mitigate the volatility and predictability inherent to outdoor test ranges, controlled environment facilities have been created for controlled, reproducible investigation of "atmospheric optics". A current popular approach to reproduce phase aberrations from turbulence is the use of a thin, aberration inducing phase screen. Phase screens allow the user to design and apply a known distortion structure to the incident beam. This can be accomplished with spatial light modulators or specially produced phase plates [18]. Yet, static phase screens do not allow for temporal fluctuations and correlations and large numbers of screens would be required to simulate path-integrated

effects.

A second facility architecture is the direct creation of laboratory-scale turbulent flows. Novel facilities such as Majumdar's multi-pass blower facility [19] and Elliot's liquid ethanol tank [20] were designed to maximize the overall optical effects over a very small spatial footprint. These facilities create similar scintillation as that seen in the atmosphere, but just like the phase screens, it is difficult to directly trace the uncertainty in turbulence parameters such as length scales and refractive index spectrum. Recently, indoor facilities that utilize thermally generated buoyancy driven turbulence have shown promise. The largest of these facilities is the David Taylor complex which spans a nearly 1 km path length. This facility creates a controlled testing environment for large propagation distances [21]. The University of Clemson's Variance Turbulence Generator (VTG) was also built in the same fashion as the David Taylor Range, except including a louvered enclosure to mitigate the influence of the laboratory HVAC system [22]. These facilities utilize resistive heat ropes to generate a consistent low-speed turbulent field throughout the entirety of the propagation length. The optical beam traverses a considerable distance above the heat rope where the turbulence is deemed to be fully developed and acceptably homogeneous. Facilities such as these are controllable and modifiable allowing the user to select the desired intensity of turbulence by adjustment of the heating intensity. However, due to the nature of the turbulence generation, there is a bulk flow in the vertical direction causing the turbulence to not be truly isotropic or precisely follow Kolmogorov scaling. This is an issue because fully developed and isotropic Kolmogorov turbulence is one of the vital assumptions made in commonly used theoretical results [5], although extended formulae are available [8]. Also, the refractive index intensity and inner scale are correlated to the applied heat rope power, making independent variation of key parameters a practical challenge. In summary, even the most realistic and predictable facility requires precise quantification of turbulent and optical parameters specific to each test range and test range condition.

This work aims to improve upon existing characterizations of an atmospheric optic test facility through the acquisition of independent measurements of turbulence parameters using both direct,

local flow measurements and optical measurements. Specifically, the objective is the connection of local or short-path measurements of turbulence parameters with longer-range beam propagation, scintillation, and wavefront scaling laws. The experiments herein were conducted in the Texas AM Subscale Atmospheric Facility (SAF) which produces buoyancy-driven turbulence via resistive heat ropes similar to the VTG and David Taylor range. The SAF is capable of uniform turbulence generation over a maximum 80 ft linear distance with controllable 10 ft sections as described in chapter 2.

This work focuses on several methods used to characterize the local and path-integrated facility parameters. This includes short-path measurements: 1) imaging of the density gradients via *in-situ* Schlieren imaging, 2) Filtered Rayleigh Scattering experiments of 2D density fields, and 3) thin beam correlation measurements of the inner scale. This set of short-path or local measurements are applied to extract key turbulence parameters which are then used for long-range propagation predictions. Specifically, path-resolved measurements of laser scintillation were conducted over a full range of turbulence intensity. The utility of these characterization methods and their applicability to other facilities is also discussed, as are potential improvements on the above procedure and methodology.

2. BACKGROUND

This chapter reviews the fundamental basis of atmospheric optics focusing on irradiance fluctuations induced by beam propagation through turbulence. The parameters affecting the magnitude and distribution of irradiance fluctuations are described and later applied toward characterization of the sub-scale atmospheric facility (SAF).

2.1 Review of Atmospheric Optics

In this work we consider the propagation of a monochromatic, coherent light source (laser) through a weakly refractive turbulent medium. Provided a small angular divergence of the beam and gradients in the refractive index over lengths much greater than λ, the wave optics description of the laser field is simplified to the paraxial wave equation [23],

$$2ik\frac{\partial E}{\partial z} + \nabla_{\perp}^2 E + k_0^2(n^2 - n_0^2) = 0, \tag{2.1}$$

where $k = k_0 n$ with $k_0 = 2\pi/\lambda$ being the vacuum propagation constant, n being the spatially-varying refractive index, n_0 being the mean refractive index of the medium, and E being the amplitude of the wave. In the absence of turbulence, a homogeneous medium attains $n = n_0$ and the free space propagation is affected only by diffraction. In this situation, there would be no temporal intensity or phase fluctuations, only changes to the overall beam profile with propagation distance. In the second case, the medium is not homogeneous but may attain a static refractive index profile $n(\mathbf{r})$ causing additional refraction of the beam. This occurs, for example, in the mirage effect. Finally, one may consider the temporal variation of the refractive index field due to turbulent motions within the flow, yielding $n(\mathbf{r}, t)$, which results in time-variation of the field amplitude commonly known as scintillation. Common examples include the twinkling of a star or heat waves coming off the ground on a hot day. Ultimately, the scintillation amplitude and frequency content relate to both the size of turbulent structures and the rate by which they evolve over the propagation path. In the following, we assume that the flow timescales are much smaller

than the propagation time L/c such that equation 2.1 can be used without consideration of the finite speed of light.

The variations in the refractive index shown in equation 2.1 are fundamentally connected to variations in air density due to turbulence. An example of this can be seen in figure 2.1, which shows an initial beam profile, a profile after propagation through free space (diffraction only), and a beam propagated through a simulated turbulent field. This figure was created using the split-step beam propagation method that takes diffraction effects into account by Fourier methods and refractive effects into account by phase screens [23]. Equation 2.1 shows that if the refractive index n is zero there are only diffractive contributions. If there is a non-zero n present in the medium, then both refraction and diffraction take effect. This method of beam profile prediction gives one an idea of how diffraction and refraction effect a beam profile.

2.1.1 Beam Intensity Fluctuations

Here we define scintillation in the usual sense as the fluctuation in amplitude or power either at a point or captured by a finite-sized collection optic, such as a receiver or telescope. The effect of scintillation on engineering applications can be significant, especially for strong turbulence and long propagation paths. This poses a challenge both for photometry in astronomical observations and drop-out of communication signals for free-space laser communication through the atmosphere. Finally, scintillation directly relates to the degradation of focusing and termination of directed energy weapons at a target[16]. After propagation through turbulence a laser beam's intensity distribution becomes distorted, as seen in figure 2.1. Thus, the understanding and mitigation of scintillation is a central issue in atmospheric optics and can be studied in laboratory settings.

As an example, figure 2.2 shows the intensity pattern of a beam within the SAF. The left image in figure 2.2 shows a beam subjected to 80 ft of ambient atmospheric conditions (heat rope powered off), and the right image is the beam profile after being subjected to 80 ft of turbulence (heat rope powered on) including a target grid. The inclusion of turbulence results in striations of light and pockets of higher and lower light intensity. These striations, consisting of focused and unfocused

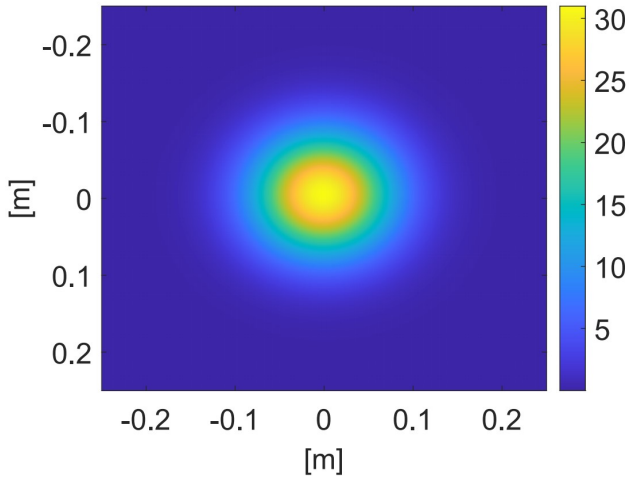

(a) Free-space propagation.

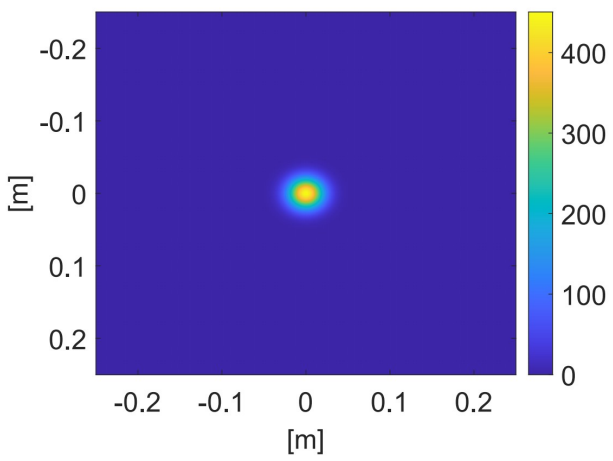

(b) Initial irradiance profile.

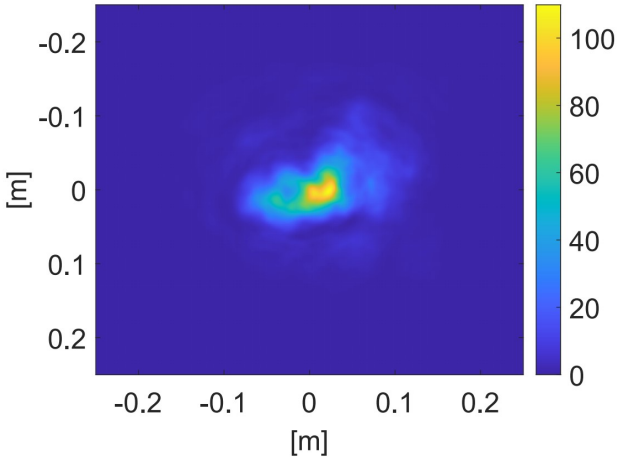

(c) Propagation with turbulence.

Figure 2.1: Beam irradiance before and after propagation.

regions, are highly variable in time and space. In the following, we aim to develop a quantitative model of the irradiance fluctuations observed in figure 2.3.

2.1.2 Understanding Scintillation in the Atmosphere

As a first pass, a heuristic description of scintillation effects in the atmosphere found in the work of Strohbehn will be used [24]. In his paper, a parallel was drawn between atmospheric eddies and weak conventional lenses. This situation is shown graphically in figure 2.3.

The next step is to relate this random field of eddies to a random distribution of lenses. To start,

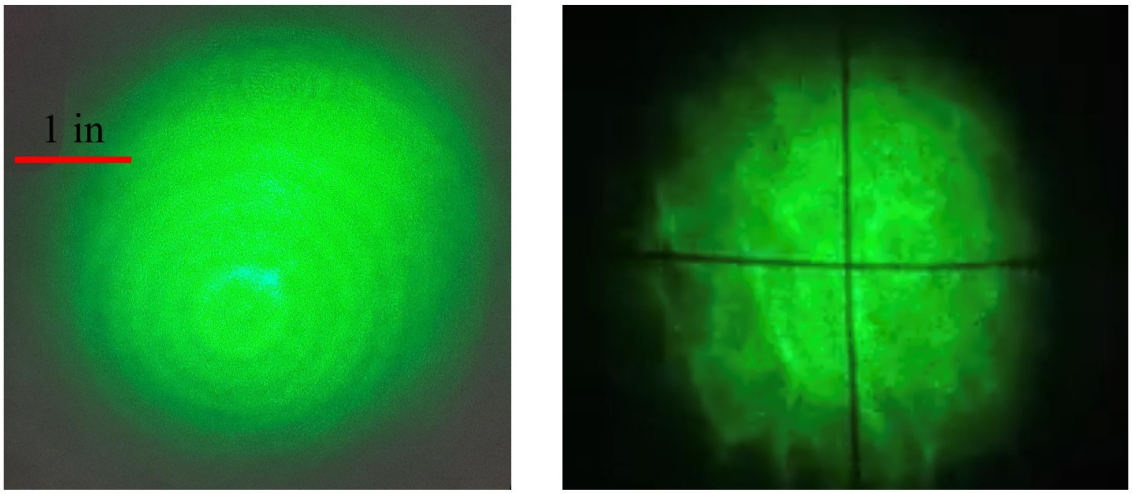

Figure 2.2: Comparison of beam profiles with and without turbulence. (a) Turbulence turned off. The airy pattern in the profile is from internal reflections off of the non-coated 8 in aspheric lens. (b) Turbulence turned on. The cross hatch is an artifact of an alignment apparatus at the SAF's end.

we only need consider the effect of a single eddy/lens on the beam. Assuming this single lens is of diameter D and has a refractive index of $\Delta n = n - n_0$. The focal length of the single lens is then,

$$F \approx D/\Delta n \tag{2.2}$$

Now assume that a plane wave interacts with this lens at a distance z from the origin. The location of fluctuation measurement is also defined to be at a distance L, as shown in figure 2.3. By energy conservation we then have,

$$A_o^2(r/2)^2 = A^2 D^2, \tag{2.3}$$

where the variable A_o is the intensity of the plane wave prior to the lens interaction, A is the intensity at L, and r is the radius of the beam at location z. Defining, $\delta A = A - A_o$, the intensity fluctuation after the lens interactions is therefore,

$$A = \frac{L - z}{F - L + z} A_o. \tag{2.4}$$

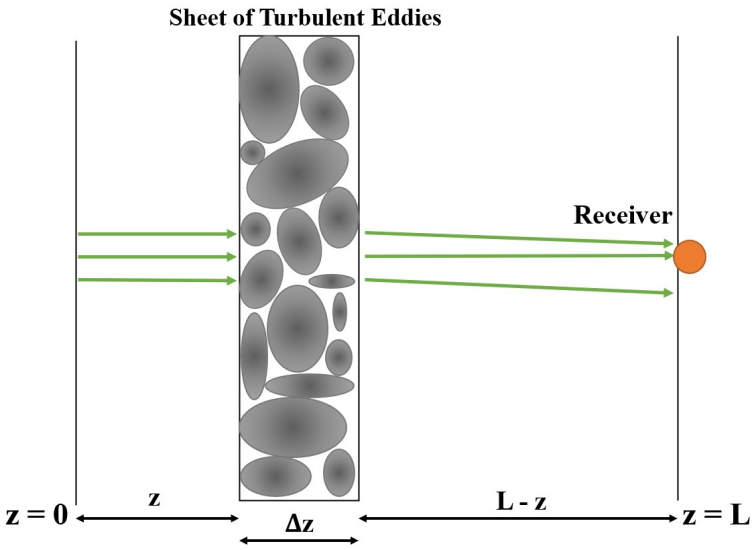

Figure 2.3: Geometric optics description of scintillation as due to a collection of eddies of various size and strength.

Since the refractive index of air is very small, the focal length of an eddy can be assumed to be much larger than $L - z$. In this limit,

$$\frac{\delta A}{A_o} \approx \frac{L - z}{F}. \tag{2.5}$$

At this point, the observed experimental turbulent parameters can be substituted for the above idealized optical parameters. In order to relate F to experiments we consider the eddies to be of diameter $D = 2r$ and the variance of the refractive index goes as the eddy size to the $2/3$ power as $\langle \delta n^2(r) \rangle \approx C_n^2 r^{2/3}$ [25]. The refractive index fluctuation can then be written as $\delta n \approx C_n r^{1/3}$. Substituting this result into equation 2.2 yields an expression for the effective focal length:

$$F = r/(C_n r^{1/3}), \tag{2.6}$$

where equation 2.5 in terms of the new focal length expression is then,

$$\frac{\delta A}{A_o} \approx r^{-2/3}(L - z). \tag{2.7}$$

It is seen from equation 2.7 that the $r^{-2/3}$ dependence implies that the smallest turbulent scale l_o will contribute the most to the amplitude fluctuations. Therefore, we can simply take $r = l_o$ as the dominant term. The resultant normalized variance of the scintillation is then,

$$\left\langle \left(\frac{\delta A}{A_o} \right)^2 \right\rangle = \sigma_I^2 \approx C_n^2 l_o^{-4/3} (L - z)^2. \tag{2.8}$$

equation 2.8 above is the averaged amplitude fluctuation for a single eddy. The left hand side is commonly referred to as the scintillation index, σ_I^2. Since the propagated beam will see a multitude of eddies along the path, it is necessary to calculate the integrated effect. At a propagated path length of L and a eddy size of l_o, it can be assumed that the beam sees a total of $N = L/l_o$ eddies. Starting with equation 2.8, the effect of multiple eddies results in,

$$\sigma_I^2 \approx C_n^2 l_o^{-7/3} \overline{(L - z)^2} L, \tag{2.9}$$

where the term $\overline{(L - z)^2}$ is the average over the path. If a prefactor of order unity is applied to the expression than $\overline{(L - z)^2} \approx L^2$. This results in a final expression given by,

$$\sigma_I^2 \approx C_n^2 l_o^{-7/3} L^3. \tag{2.10}$$

This derivation of scintillation with respect to atmospheric turbulence parameters came with the assumption that only geometric or refractive optics was influencing intensity fluctuations. While this assumption is valid in the near field, in the far field diffractive effects begin to contribute to intensity fluctuations as well. This first pass derivation is useful to understand the dependent parameters of atmospheric optics. A more rigorous approach described by Tatarskii will now be presented in order to understand the transition between the refractive, diffractive, and "deep turbulence" regimes [5].

2.1.3 Scaling Regimes

In the rigorous wave-optics theory of atmospheric optics, Tatarskii derived the near-field and far-field regimes, pre-factors, and scaling of scintillation statistics to be [5],

$$\sigma_\chi^2 = 12.8 C_n^2 l_o^{-7/3} L^3, \quad l_o^2/\lambda >> L \tag{2.11}$$

$$\sigma_\chi^2 = 1.23 C_n^2 k^{7/6} L^{11/6}, \quad L_o^2/\lambda >> L >> l_o^2/\lambda \tag{2.12}$$

The saturation regime is approximated by [10],

$$\sigma_\chi^2 \approx C_n^2 k^2 L, \quad L >> L_o^2/\lambda \tag{2.13}$$

These relationships were derived assuming the Rytov (perturbative) approximation of plane wave beam propagation interacting with a Kolmogorov type turbulence environment. The refractive index structure constant, C_n^2, parameterizes the strength of refractive index fluctuations following a Kolmorogov scaling. In the simplest case considered here, the scaling laws are valid when C_n^2 is constant throughout the entire propagation distance. Equation 2.11 corresponds to the geometric optics regime, where there are no diffraction effects even from the smallest eddy. Equation 2.12 takes both refraction and diffraction in to account, where the smallest eddies are in the diffractive regime and larger eddies still inhabit the geometric optics limit. Finally, equation 2.13 occurs in the saturation of scintillation or 'deep turbulence' regime. As observed from the transition factors, the Fresnel number corresponding to characteristic eddy scales is used to determine the transition between the L^3, $L^{11/6}$, and L^1 scaling regimes. The Fresnel number $F(a)$ proposed with atmospheric optic parameters is defined as,

$$F(a) = a^2/\lambda L, \tag{2.14}$$

where a is a characteristic length scale. In a small-scale laboratory setting, one need only consider the smallest turbulent eddy because these have the largest impact on the scintillation (see section 2.1.2) and will transition to the diffractive regime first. If $F(l_0) << 1$ the beam can be approximated to be in the far field and diffraction effects are present. If $F(l_0) >> 1$ all scales of turbulence are in the geometric optics regime. It is apparent from equations 2.12 and 2.11 that a beam propagating through a homogeneous turbulent field with constant values of C_n^2 and turbulent length scales will see a significant reduction in scintillation growth after a distance of $L = l_0^2/\lambda$ where we see the transition $L_{3\to 11/6}$. This scaling regime transition is dependent on the monochromatic beam's wavelength as well as l_o. As a result, the distance $L_{3\to 11/6}$ is specific to the characteristics of both the turbulence and laser source.

The transition between the $L^{11/6}$ and L regimes is dependent on the Fresnel number of the largest eddy $F(L_0)$. At propagation distances of this size the dominant length scales contributing to scintillation are on the order of the largest integral length scales, L_o. At very far propagation distances the effects of the small eddy's convect quickly across the beam profile. The large slower moving eddies of scale L_o persist for longer and have an overwhelming effect on the scintillation. Although the eddies of the size of the Fresnel zone still have the greatest effect on the diffraction pattern of the beam, this aberration is not comparable to the effect the larger slower moving eddies have [26].

2.1.4 Application to the SAF

It has been shown that scintillation is dependent on the path length, turbulent structure, turbulent strength, and laser wavelength. These many dependencies make scintillation a particularly useful tool for characterization of the aero-optical environment. As will be shown through subsequent measurements, the inner scale in the SAF is on the order of five millimeters, and the maximum propagation distance $L = 24.4$m. This results in a transition $L_{3\to 11/6} = l_o^2/\lambda = (5\text{mm})^2/532\text{nm} = 47\text{m} > 24.4\text{m}$. Therefore, the transition out of the geometric regime should be further than the 80 ft (24.4 m) length of the facility. Equation 2.10 also assumes that C_n^2 and the turbulent length scales are constant throughout propagation which is the case for uniform turbulence generation

throughout the SAF. Provided this is enforced during the experiments, equations 2.10 and 2.11 are applicable to the SAF testing environment.

In the following sections, we report on a series of experiments designed to independently extract and decouple the effects l_o, C_n^2, and L have on the observed amplitude fluctuations, $\langle (dA/A)^2 \rangle$. The SAF was designed knowing *a priori* that the quantification of these parameters was essential to understand the test environment. For instance, by implementing numerous access points along the propagation path, distance scaling laws can be found within the facility. Also, the intensity of turbulence in the SAF can be varied in a controlled manner, creating uniform C_n^2 and l_o along the facility length. The specific capabilities of the SAF and their utility for characterization will be described in the following section.

3. FACILITY AND TURBULENCE GENERATION

3.1 Test Facility

* The SAF design allows for the ease of implementing diagnostic procedures as well as the versatility to execute a variety of experimental setups. The enclosed and controlled environment of the SAF also allows for the repeatability of test conditions. The base structure of the SAF is composed of 8 individually mounted, 10 ft long and 2 ft inner diameter painted carbon steel tubes. Each tube is mounted on a movable cart, allowing for easy reconfiguration of the system. This 80 ft long facility is located indoors at the Texas A&M Aerospace Laboratory for Lasers, Electro-Magnetics and Optics (ALLEMO). Along with the enclosed propagation tunnel, an 18 W Verdi CW laser, high-speed cameras, large 8 inch diameter collimating optics, Shack-Hartman type wave front sensors, and a constant temperature anemometer are available for use. The ability to section the facility every 10 ft allows for the insertion of octagonal access sections. These sections allow optical and physical access to the interior of the SAF at various propagation distances.

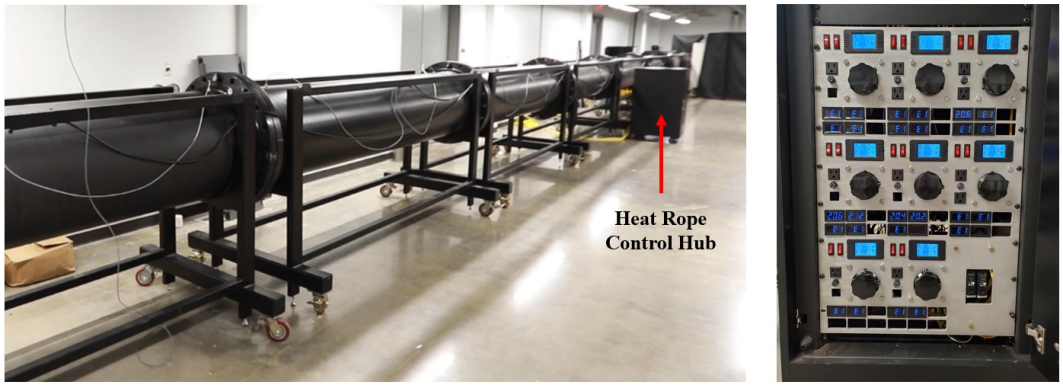

Figure 3.1: The left image is of the SAF assembled within Texas AM's ALLEMO long-lab. The heat rope control hub can be seen in the left image as well as by itself in the right image.

*Part of this chapter is reprinted with permission "Laser Scintillation Measurement in a Controlled Turbulent Environment" by Grant Erickson, James Creel, Richard B. Miles and Christopher Limbach, 2022. AIAA 2022-0985 Session: Aero-Optics and Atmospheric Optical Turbulence Published Online:29 Dec 2021.

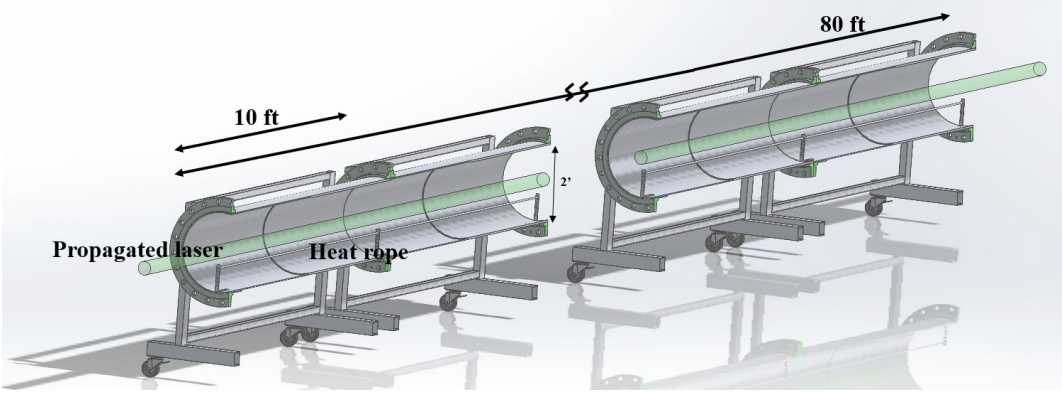

Figure 3.2: A schematic to show the dimensions and interior of the SAF.

To generate low speed turbulence mimicking the atmosphere, each tube is outfitted with a resistive heat rope that spans the length of the tube (OMEGALUX Rope Heaters, Omega, Norwalk, CT) . This turbulence generation technique is similar to that implemented in the David Taylor range and VTG facility at Clemson university [21] [22]. The heat rope can be seen in figure 3.2 strung across the bottom centerline of each tube. When powered, the rope heats up the air around it, creating buoyancy-driven flow. The SAF has the ability to continuously vary the heat rope power. By injecting more energy into the flow, the temperature gradients can be controlled to create a stronger turbulent flow field. The heat ropes are controlled at a control hub designed by Dr. James Creel. This assembly can be seen in figure 3.1. The hub contains variable transformers to independently control the voltage applied to each tube's heat rope. The Omega heat ropes are capable of 4 Watts/in of power density and $900°F$ maximum temperature. To increase or decrease the turbulent intensity within the SAF, the user adjusts the power supplied to the heat ropes as observed on digital readouts of the voltage, current and power supplied to each tube. There are also thermocouple readouts displayed on the control hub corresponding to a multitude of probed stations within the SAF. The thermocouples are K type with a fiberglass covering and metal lead. They are mounted approximately 3 inches above the heat rope at each entrance and exit of a SAF tube with via a stiff wire guide epoxied to the surface of the tube. All of these features allow the control hub to provide a live status of the test environment during experimentation.

When testing at outdoor ranges, the user is limited to certain propagation distances and is subject to environmental and weather effects of which they have no control. During outdoor testing, the turbulent environment can also change quickly. Therefore, the turbulent characteristics for a given test must be quantified at exactly the same time as the beam propagates [12]. Within the SAF, the turbulence forcing is controlled and reproducible from which we may assume, and later verify through measurements, that the turbulence characteristics can be reproduced during subsequent tests. Although the previous statement may hold for most indoor facilities, what makes the SAF advantageous is the capability to conduct a wide range of testing scenarios. For instance, the SAF can be sealed off from ambient conditions and brought to lower than atmospheric pressures to simulate higher altitudes of propagation. Another test condition is to inject various density gasses into the SAF to simulate laser propagation through colder or hotter environments. Also, a cross-flow generator capable of speeds up to 25 m/s can be attached to the SAF to simulate laser propagation in a moving environment. In this work the low speed buoyancy-driven turbulence was of primary interest although all of the techniques described herein have wide applicability.

3.2 Qualitative Analysis of the SAF's Buoyancy Driven Turbulence

It is imperative to first understand the overall structure, time scales, length scales, and qualitative characteristics of the resistive turbulence generators placed within the SAF.

In order to obtain a qualitative assessment of the turbulent structure produced within the actual facility at various conditions, Schlieren imaging was conducted within a single SAF section. Schlieren visualization is a technique sensitive to density gradients present within a flow field. Variations in density can be caused either by adiabatic compression (as in high-speed flow environments) or by temperature variations at nearly constant pressure. Both regimes produce variations in the index of refraction of the medium which is linearly connected to the density through the Gladstone-Dale constant. These variations cause light to be steered in different directions as by a prism. Referring to the schematic of a double pass Schlieren setup shown in Figure 3.3, light passed through the field of interest is reflected and focused back by a concave mirror. A sharp blade is inserted at the focal point of the returned light, clipping a majority of the reflected image

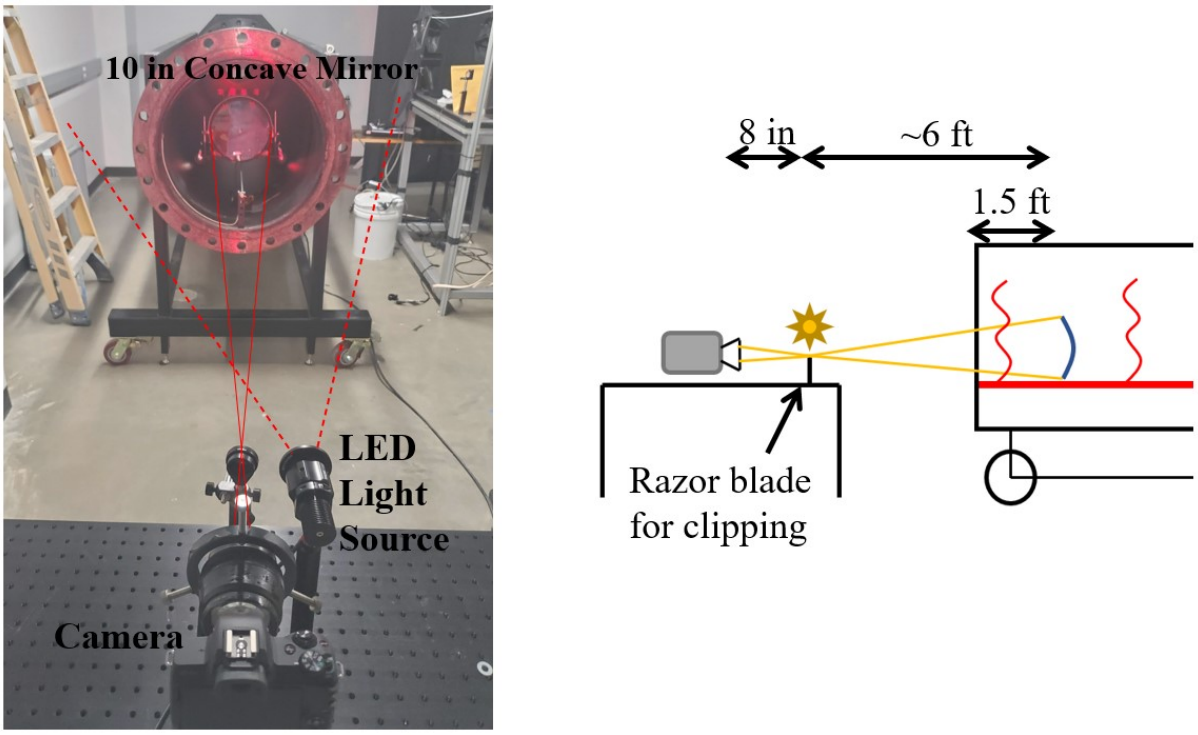

Figure 3.3: The left image is of the actual Schlieren setup. Overlaid is the light path onto and from the 10 in concave mirror. The right schematic is a schematic of the experimental setup denoting the clipping optic placed at the focal point of the large mirror.

of the light source. Some of the light that is refracted by the density gradients within the medium is diverted onto the clipping blade. This blocked light does not reach the imaging camera. The resulting image then contains higher or lower intensity regions corresponding to the regions of varying density gradient [27] [28] [29]. Although physical quantities such as turbulent length scales and density cannot be accurately obtained through this method, Schlieren provides a convenient qualitative assessment of the turbulent field.

Schlieren imaging was conducted within the SAF using a large 10 inch concave mirror placed at approximately the center line of a propagation tube. The mirror was positioned above the heat ropes in order to capture the developing turbulent plume as it propagated through the field of view. A diverging light source (ThorLabs, 700nm, Mounted LED) located on an optical table approximately 6 ft away was directed through the turbulent field and onto the concave mirror. The reflected light was focused to approximately the same location as the original light source by

slightly offset. A razor blade was placed at the focal point of the redirected light to provide the Schlieren cutoff and blocked a majority of the incoming light. After the light was cut by the blade, it was then imaged through a Zeiss Milvus 2/100M lens (Zeiss, Oberkochen, Germany) onto a mirrorless Canon EOS R digital camera (Canon, Tokyo, Japan).

The resulting images can be seen in figure 3.4. Schlieren imaging was conducted at increasing heat rope powers of 6, 24, 50, 88, and 136 W/m. These power settings were chosen to be 40%, 60%, 80%, and 100% of the total voltage that could be applied to the heat ropes. The incremental increase of the heat rope power was motivated by determining the effect increased power had on the turbulent structure. It was found in testing that the the density gradient at higher heat rope power and represented by the imaging was more drastic, moves at a faster rate, and contained smaller turbulent eddies. This is as expected due to the fact that more energy is being input into the flow. Schlieren was also utilized to determine the directional homogeneity of the flow. Understanding the homogeneity will prove useful in comparison to theoretical models. To determine if the flow field contained directionality, experiments were conducted with the knife edge of the Schlieren setup oriented vertically and horizontally. Orienting the blade in a certain direction makes the Schlieren experiment sensitive to the gradients in refractive index perpendicular to the blade edge. As you can see in figure 3.4, the two directions contain a different structure. This shows that the turbulent field created within the SAF is not self-similar in the transverse and vertical directions. The buoyancy driven flow has a dominant component in the vertical direction that has not mixed and become symmetrical in structure at the location of the beam.

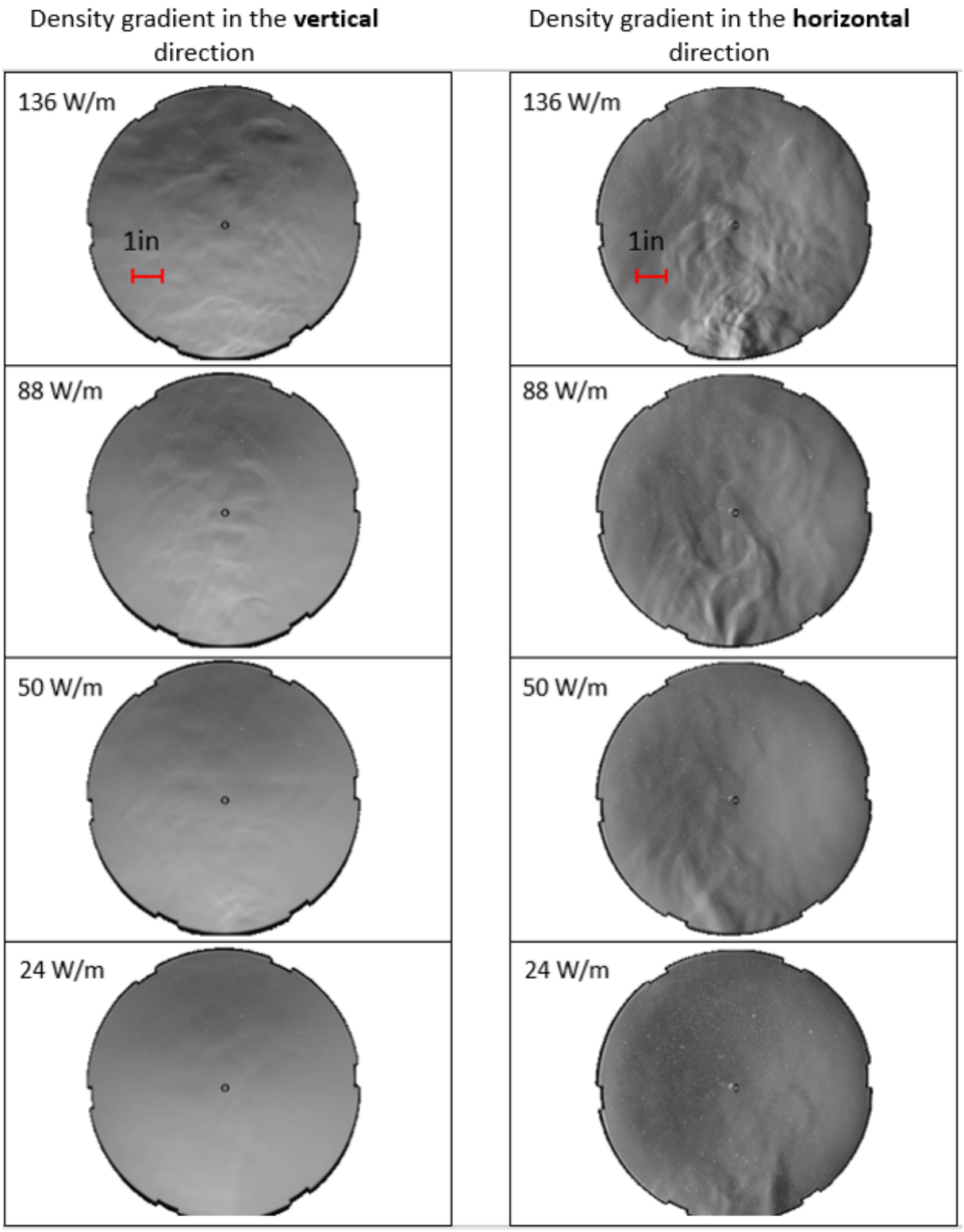

Figure 3.4: Schlieren images of turbulent plume. Left cross-sections are of vertical gradients in air density, right cross-sections are of horizontal gradients. The top most images are the result of a 136 W/m heat rope setting and the next 3 are of 88 W/m, 50 W/m, and 24 W/m respectively. The black circle in the middle of the images is an artifact of the large diameter concave mirror.

4. INNER SCALE: PARALLEL BEAM CORRELATION

4.1 Background

The Schlieren test qualitatively predicted that as the heat rope power is increased, the turbulent length scale decreases. While this was useful information to help design experiments, the Schlieren representation of the turbulence is not quantifiable. In attempt to derive mathematical relationships of parameters, the turbulence produced by the heat rope needs to be quantitatively measured. Seen in figure 3.4, both the turbulent intensity and geometric turbulent structure are effected by increasing the heat rope power. This denotes that the turbulent length scale and turbulent intensity are coupled and cannot be independently controlled with the turbulence adjustment method within the SAF. The following experiment was designed to decouple these two parameters and find the dependency of turbulent length scales on the magnitude of the heat rope power. First, a overview of turbulent energy transport and turbulent length scales will be discussed as well as how these features are leveraged in the experiment to come.

4.1.1 Turbulent Length Scales

When energy is input into a viscous fluid the flow field progresses into a chaotic and variable distribution of velocity, density, and energy. Due to the interaction of particles with their neighbors, energy is transported throughout the flow until eventually dissipating as heat. This transferal of energy is what creates turbulence. Turbulent fields are difficult to predict due to the nonlinearity of the governing Navier Stokes equations as well as their chaotic nature. A small provocation of flow conditions on one side of a turbulent flow field quickly propagates throughout the field inducing highly unpredictable quantities everywhere [4].

The process of energy transport through a turbulent flow is well understood. Atmospheric turbulence follows what is commonly referred to as the energy cascade. This phenomenon is graphically depicted in figure 4.1. Energy is input into the system at the largest scales, or largest eddies (L_o). Due to the dissipative nature of turbulence and the second law of thermodynamics, the initial

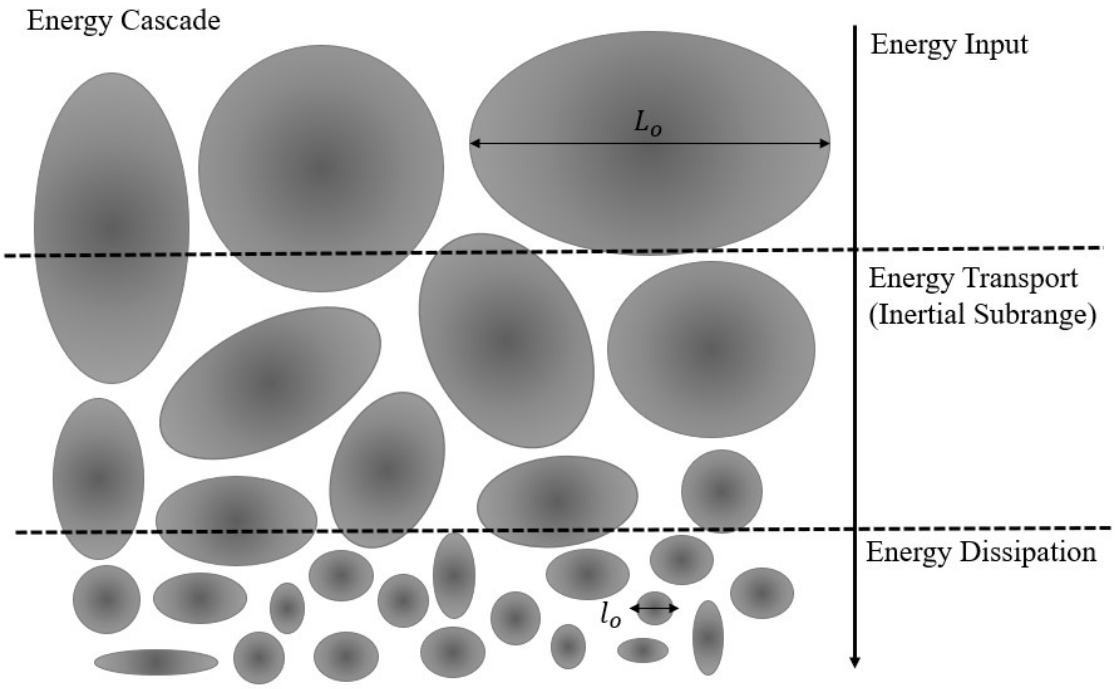

Figure 4.1: Turbulent eddy energy cascade. Energy is input at the largest scales, is transported through the intermediate scales, and then dissipated into heat at a finite inner scale.

input energy is driven to an equilibrium throughout the flow. As a result, smaller turbulent length scales are created to transfer this energy towards the ideal state of uniform energy distribution. This transitional regime is dominated by inertial effects within the flow, and is therefore referred to as the inertial sub-range. In this range of eddy sizes, energy is neither created nor dissipated. The final stage of the energy cascade is the dissipative regime. Once the energy transport eddies have reached a scale small enough, the energy within the eddy is directly dissipated to the particles in the flow as heat. This lower bound of eddy size occurs at the length scale in which viscosity dominates dissipation. The energy is then converted into heat. This regime is defined by the parameter of the inner scale (l_o). The turbulence scales within the SAF are therefore bounded between the largest scale L_o and the finite yet smallest scale l_o specific to the facility and turbulence generation therein.

In the actual atmosphere the size of turbulent eddies can vary from multiple kilometers at the largest scale to a few millimeters at the smallest [30]. Determining the distribution and energy

content within each turbulent eddy regime at the atmospheric scale is one of the biggest challenges facing atmospheric optics today. This large range of scales creates complexity in modeling and predicting the effect turbulence has on light propagation. As described in chapter 2 in section 2.1.3, the effects an eddy has on a propagated beam is dependent on the eddy's size. The SAF's fluid structure sizes are limited by the dimensions of the facility and the viscosity of the flow. Therefore, this facility contains a more simplified environment in comparison to the atmosphere for modeling AO phenomenon. Although, laser propagation through the the SAF can be compared to laser propagation through atmospheric turbulence in the near field. It will be shown in chapter 6 that the SAF behaves in agreement with the near field regime. In the proof proposed by Strohbhen, it was shown that the the inner scale is the most influential to a propagated beam's intensity fluctuations in the near field[24]. Therefore, the larger kilometer scale eddies that are not able to be recreated within the SAF are not important. The largest scale eddies have little effect on the near field propagation regime. As long as the inner scale within the SAF is comparable to that of the actual atmosphere, the effect turbulent structure has on light propagation in the atmosphere can be recreated within the SAF. As a result, the inner scale in the SAF needs to be characterized. Finding the influential inner scale will be the focus of the next experiment.

4.1.2 Extracting the Inner Scale

The only mechanism present within the SAF to adjust the magnitude of l_o is the power applied to the heat rope. It will be shown in chapter 5 that the heat rope also effects C_n^2. In order to decouple l_o from C_n^2 the underlying physical mechanisms of these quantities must be understood. Firstly, the refractive index structure constant C_n^2 is dependent on the gradients of density within the flow. This parameter will be explained in more detail in the subsequent chapter 5. The inner turbulent length scale in the near field effects the propagated beam in a manner that can be described using geometric optics principles. A propagated beam is disturbed with respect to the geometric size of the eddy as well as the location in which it encounters the eddy. An experiment developed by Consortini will now be proposed that singles out geometric discontinuances while leaving dependencies of gradient magnitudes alone[15]. Her method will first be explained and

then implemented within the SAF.

Consortini's inner scale isolating experiment exposes the effect a turbulent field has on the spatial fluctuation, or jitter, of a laser beam [31]. Atmospherically induced beam jitter is an intensity fluctuation effect caused by the same underlying principles as scintillation. The only difference between the two is that instead of a beam profile being effected non-uniformly by eddies of a size smaller than that of the beam diameter (the case of scintillation), eddies of the size of the beam diameter synchronously shift the entire profile. When a beam encounters a turbulent eddy of a size comparable or smaller then that of the beam diameter, the beam is focused as if passing through a lens. When a beam encounters an eddy that is larger than the beam diameter, the entire beam profile is shifted as if the beam interacted with a prism. Atmospherically induced beam jitter impacts thin beams more so than large diameter beams as thin beams are more likely to be smaller than a majority of the turbulent structures within the flow. If a beam's diameter is comparable to the size of the inner scale only jitter will occur with minimal scintillation in the near field.

Consoritni's method begins by co-propagating 2 thin beams through a turbulent field of interest. For the SAF implementation of this experiment, the beam diameter was 2 mm and the turbulent field was a single SAF tube with the heat rope powered to 6, 24, 50, 88, and 136 W/m. The goal of the experiment within the SAF is to extract a heat rope power dependent measurement of l_o within the actual SAF environment. The beam's diameter is assumed to be much smaller than the smallest turbulent scale. This assumption predicts that the beam will only be effected by jitter. Due to the beams propagating through turbulence, jitter is induced in both the vertical and horizontal directions. The magnitude and direction of the jitter is dependent on the path the laser took through the turbulent medium as well as the distance of propagation. When the two beams are initially very close together, lying in relatively the same turbulent path, the two beam's jitter becomes highly correlated in the both the horizontal and vertical direction. This is indicative that the two beams are seeing relatively the same turbulent field, or are at a distance from each other that is within the smallest turbulent scale l_o. Figure 4.2 shows a graphical representation of the co-propagted beams. As the distance, d, between the two beams is increased, the correlation between

the beams begins to decrease. However, note that the experiment is set up in such a way that the distance between the co-propagated beams is only changed in the y direction. The plane normal to the x direction is maintained. Because of this shared plane, the correlation of beam jitter in the x and y directions will be different in magnitude and different in rate of change as the distance between the two beams is increased [31].

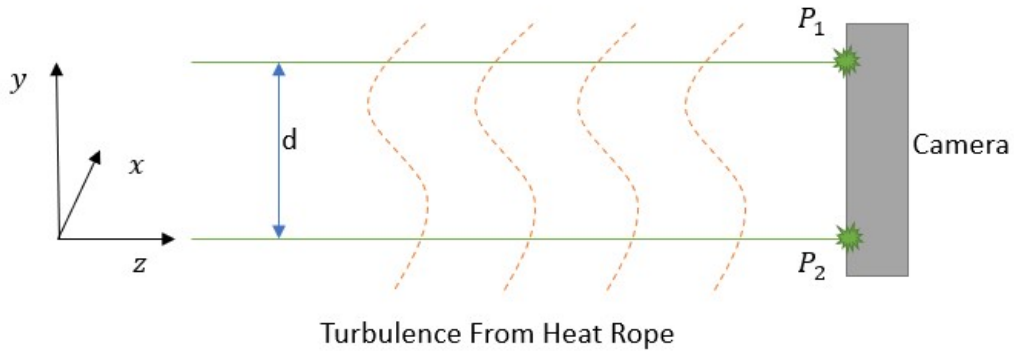

Figure 4.2: Coordinate system definition for Consortini's inner scale extraction experiment.

To describe this difference in directional correlation further, note that not all turbulent eddies are spherically symmetrical. Eddies vary in dimension in the transverse and vertical directions. Therefore a beam's jitter as an effect of turbulent interaction is dependent on the size of the encountered eddy as well as the location in which the beam intersects the eddy. Framed in the terms of this experiment, if the two beams share the initial spatial dimension x, they will be more highly correlated in the direction normal to the shared dimension (x direction) then compared to the beams correlation in the variable dimension (y dimension). This effect is what is leveraged in Consortini's method. Because the 2 parallel beams share the x dimension at the entrance into the turbulent field, the two beams jitter in the x direction will maintain a higher level of correlation for longer. Since the y dimension of the two beams is changed, the correlation of the two beams in that y direction will decrease quickly. As a result, the in plane and out of plane correlations will diverge at different

rates [31].

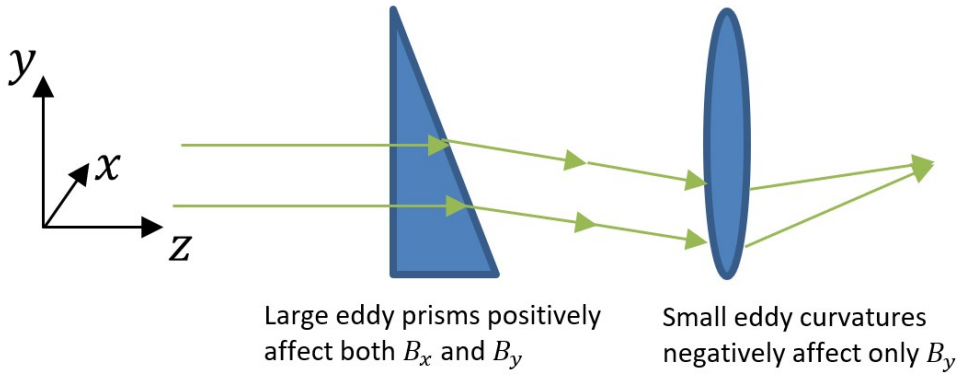

Figure 4.3: The directional correlation contribution of large and small eddies on two thin co-propagating beams.

To extract the inner scale from this plane dependent correlation recall the earlier discussion on turbulent scale dependent effects. Note that the out of plane, shared dimension x, will only be affected by the large scale features. This is shown in the left eddy of figure 4.3. The y direction, varied dimension, will be effected by the larger prism-like eddies as well as the smaller lensing eddies. As distance between the two beams begins to approach the diameter of the smallest turbulent eddy/lens the two beams begin to diverge from one another in the direction of separation. This is shown in the right eddy of figure 4.3. After the distance between the two beams, d, becomes larger than l_o the directional jitters return to digressing at approximately the same rate. The initial distance between the two co-propagated beams, d, that results in the largest difference between the in plane and out of plane correlation measurements can therefore be considered a good estimate of the size of the turbulent inner scale. At this distance, d_o, the in plane dissimilarity is being exacerbated by locking on to the lensing effects of l_o sized eddies in only one spatial dimension.

4.2 Experiment

The experimental setup shown in figure 4.5 began with splitting a low power Helium-Neon (HeNe), 543 nm wavelength laser (Newport, Irvine, CA) into two independent paths at the entrance

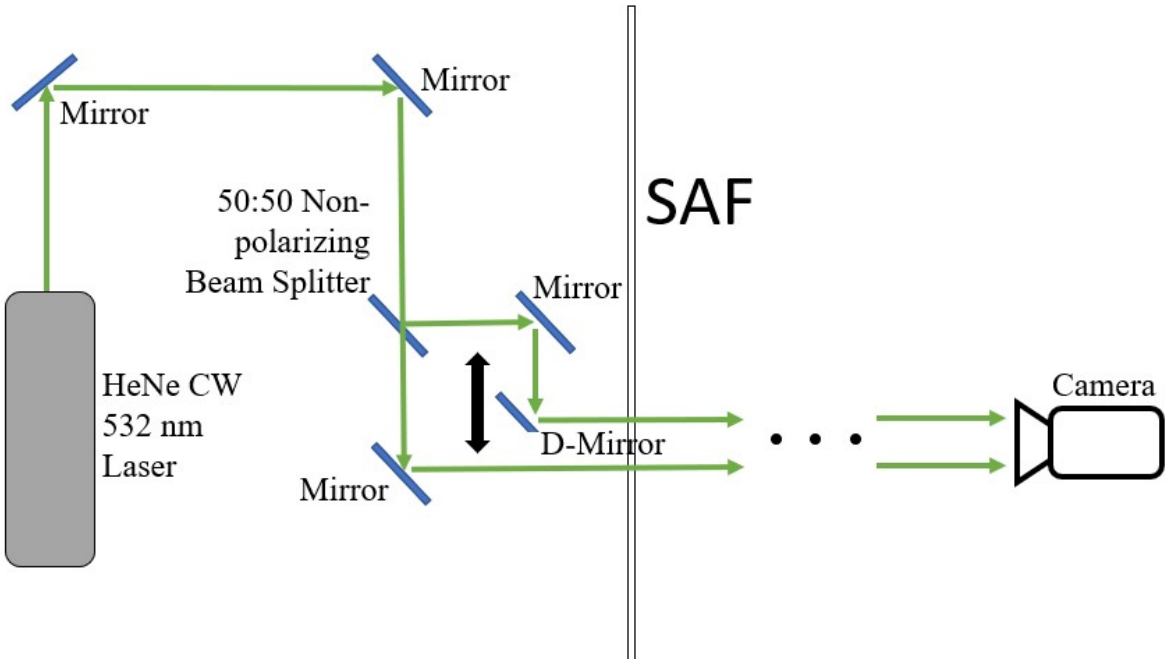

Figure 4.4: Optical layout for parallel beam correlation experiment.

to a heat rope outfitted tube of the SAF. This inner scale estimation was able to be implemented directly in the SAF turbulent environment. Furthermore, this method does not rely on probing the air with a physical apparatus that could impede the turbulent field. Also, the parallel beams were propagated along the exact path as the larger collimated beam used for the scintillation experiment described in chapter 6. Due to the non obstructive design and similar spatial location between the inner scale and scintillation experiment the turbulence environment in the two cases can considered equivalent.

Seen in figure 4.5 the optical mechanics were set up so that the distance, d, between the two beams could be accurately adjusted and monitored with a translation mount. During experimentation the out of plane separation was held constant. A D-shaped mirror was used to redirect one of the split beams as close as possible without interfering or clipping the neighboring beam. This allowed for an initial separation distance on the order of one beam diameter (2 mm). This is well below inner scale values shown in the similar VTG range which were on the order of 5mm [22]. Therefore the geometry of the experimental setup is not a limiting factor in extracting the small

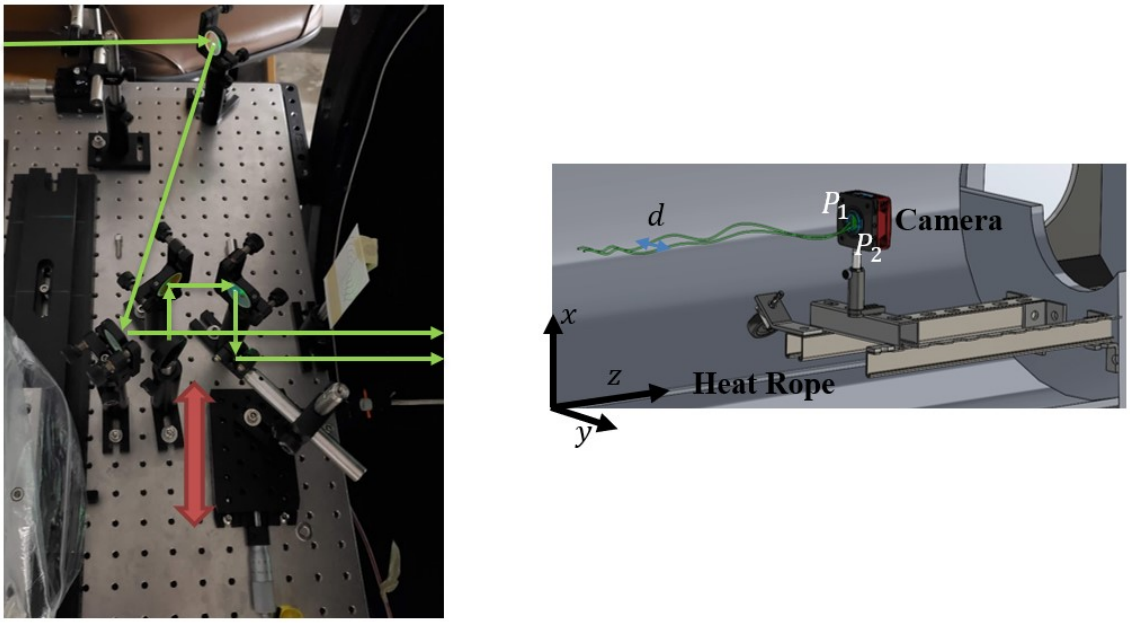

Figure 4.5: Left image is the beam path at the head of the SAF. The right image is a model of the beam collection apparatus. The coordinate system and separation distance d are defined. The rig shown in figure 6.3 was used in this experiment to reach the desired 1.8m of propagation distance.

l_o scale. The heat rope was then powered on and the flow field was allowed to reach steady state. The beams were then projected through the turbulence and onto a CMOS 1000Hz camera (Basler, Ahrensburg, Germany) after 1.8m of propagation. Due to the very small beam diameter of the HeNe laser, at distances further than 1.8m the beams began to diffract into the profile of their neighbor. The diffraction limited the measurement accuracy due to the difficulty of distinguishing between the two profiles in post processing. As a result, the measurement was taken at a short distance of 1.8 m. After propagation, the beam profiles were imaged. It was found that 1500 images at each distance, d, was sufficient to derive smooth correlation statistics. These images were taken at in plane separation distances varying from 2.5 mm to 16 mm at the head of the SAF. The experimental procedure was repeated at 6, 24, 50, 88, and 136 Watts/m heat rope power to directly compare this data set to the scintillation and C_n^2 experiments.

4.2.1 Post processing

To begin the image processing procedure, each image was input into an iteratively weighted centroiding algorithm [32]. As seen in the example image in figure 4.6 the two beam profiles contain asymmetries and impurities making the centroid finding a non-trivial task. This algorithm fits a Gaussian distribution defined by the location of the distributions approximate center and full width half max (FWHM) waist size to the irradiance image. The overlaid profile is then iteratively adjusted based off of the statistical moments of pixel intensity contained in the image data. This adjustment is continued until a centroid is converged upon. The algorithm allows for the spatial fluctuations of the beam to be tracked accurately at a sub-pixel scale. This centroiding procedure was repeated for each beam on each picture. As a result, accurate in plane (y direction) and out of plane (x direction) beam centroid shifts were located.

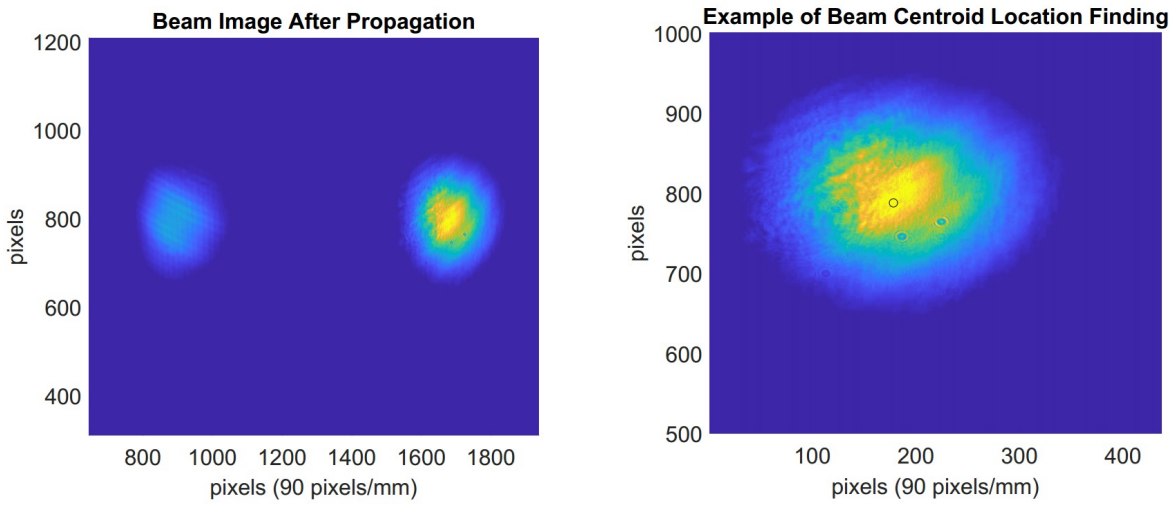

(a) (b)

Figure 4.6: Parallel beam images.

Using the defined centroids, the beams within each image are then spatially correlated to one another. Since both beams are imaged on the same camera at the same time, the temporal dependency of correlation is mitigated. The spatial fluctuations are defined in the following manner for

beam P_1 and P_2, [31],

$$n_1 = \bar{x}_1 - x_1, m_1 = \bar{y}_1 - y_1 \tag{4.1}$$

$$n_2 = \bar{x}_2 - x_2, m_2 = \bar{y}_2 - y_2. \tag{4.2}$$

Using the above notation, the correlation functions of the in plane and out of plane fluctuations between the two beams are then,

$$B_x(P_1, P_2) = \langle n_1 n_2 \rangle \tag{4.3}$$

$$B_y(P_1, P_2) = \langle m_1 m_2 \rangle. \tag{4.4}$$

The quantity of interest is the maximum difference between B_y and B_x as a function of the separation distance, d.

$$\Delta(d) = B_y(d) - B_x(d) \tag{4.5}$$

The quantities $B_x(d)$, $B_y(d)$, and $\Delta(d)$ can then be plotted against d. In order to get an accurate trend line superimposed on the data, the fit was derived using a series of hypergeometric functions derived from the Von Karman spectrum of turbulence [33]. These fits were shown by Perez to represent the physics of the problem. The equations for the fit approximation are shown below:

$$B_x(d) \approx I_1(d) - I_2(d) \tag{4.6}$$

$$B_y(d) \approx I_1(d) \tag{4.7}$$

$$I_1(d) = \frac{\pi^2}{3} A L^3 k_m^{1/3} \sum_{n=0}^{\infty} \frac{(-1)^n}{n!} \left(\frac{k_m d}{2}\right)^{2n} U(11/6, 5/6 - n, \frac{k_o^2}{k_m^2}) \tag{4.8}$$

$$I_2(d) = \frac{\pi^2}{6} A L^3 k_m^{1/3} (k_m d)^2 \sum_{n=0}^{\infty} \frac{(-1)^n}{n!} \left(\frac{k_m d}{2}\right)^{2n} U(11/6, -1/6 - n, \frac{k_o^2}{k_m^2}) \tag{4.9}$$

The term $k_o = 1/L_o$ is the inverse of the integral length scale, L_o. Also, $k_m = 5.92/l_o$ and $A = 0.033 C_n^2$. It should be noted that this fitting function takes inner and outer scales into account as well as assumes homogeneous turbulence. It is seen in the Schlieren images that the turbu-

lence created within the SAF has different characteristics in the vertical and horizontal directions. Therefore, the x direction and y direction correlations under the same influence of the heat rope power were fit using different values of k_o and k_m. The values used for k_o and k_m were chosen to minimize the χ^2 between the fit and actual data using equation 4.10.

$$\chi^2 = \sum \frac{(I_1(l_o, L_o) - B_{x/y:data})^2}{B_{x/y:data}} \tag{4.10}$$

The minimal value in the 3 dimensional χ^2 surface plot shown in figure 4.7 is the combination of fitting parameters (l_o and L_o) that result in the best fit model. It should be noted that the turbulent scales used for the best fit lines should not be taken as actuality. This numerical model was used to recreate the structure of the fit to a higher degree of accuracy than a method such as least squares could achieve.

4.3 Results

The results of the experiment are shown in figure 4.8. The subplots of figure 4.8 contain the experimental data overlaid with the hypergeometric fitting functions described in section 4.2.1. The difference between the models ($B_y - B_x$) was then calculated and plotted on the figures. The distance d at which $B_y - B_x$ reaches a maximum is plotted as the dotted red line. This distance d is indicative of the inner scale l_o dependent on heat rope power setting.

As predicted, figure 4.8 shows that the out of plane correlation (B_x) is greater than that of the in plane (B_y) for all heat rope power cases. The dissimilarity in correlation magnitude is indicative that there are various turbulent eddy sizes present within the flow and that the eddies are asymmetrical. There is also a prominent maximum $\Delta(d)$ that defines the estimated inner scale value.

It can be seen in figure 4.9 that the inner scale is inversely proportional to heat rope power. This experiment quantitatively proves what was qualitatively seen in the Schlieren images (figure 3.4). A finer turbulent structure is created as more energy is input into the flow. Further affirmation in the test results lies in the fact that the inverse proportionality to heat rope power was also seen

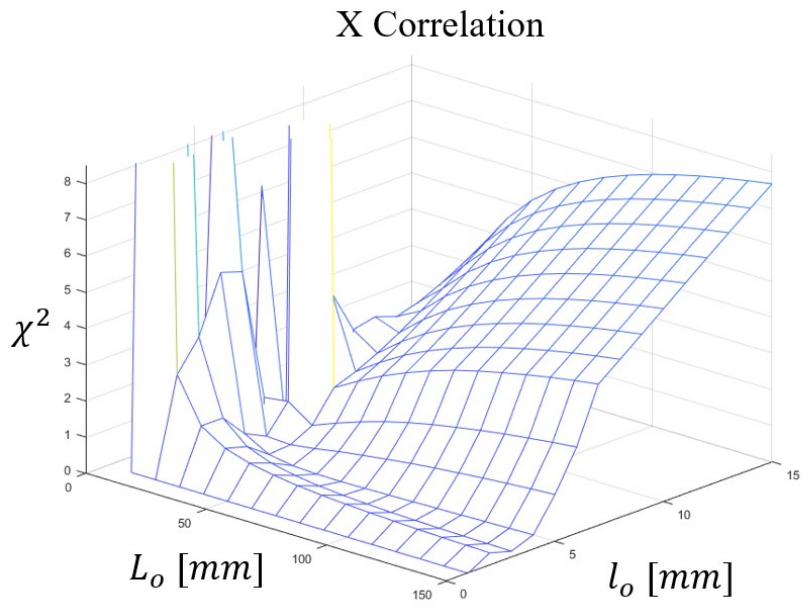

(a) χ^2 of the x direction jitter correlation at a range of fitting parameters

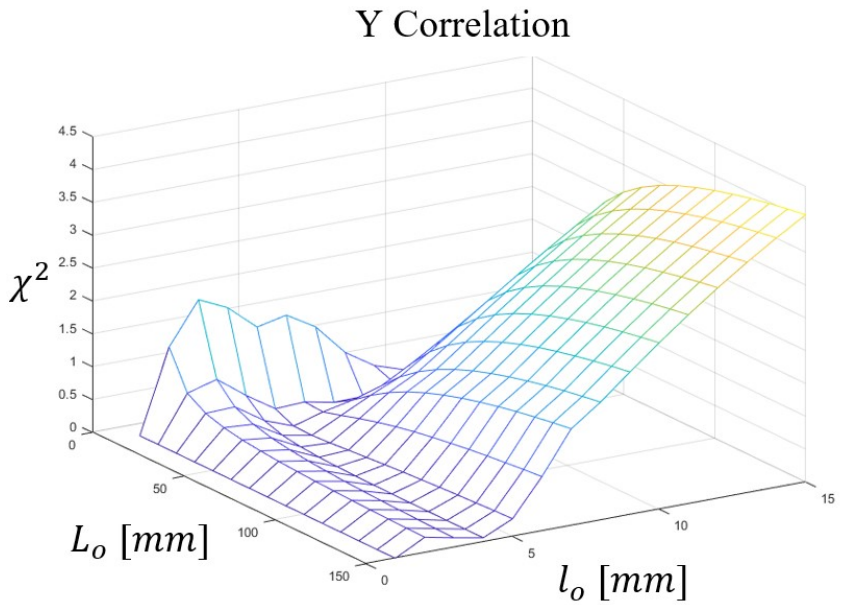

(b) χ^2 of the y direction jitter correlation at a range of fitting parameters

Figure 4.7: Meshes of χ^2 as a function of the data and fitting functions. The combination of l_o and L_o that resulted in the lowest χ^2 value was used in the model.

in Clemson's VTG facility characterization study [22]. With the calculation of l_o values specific to the SAF conditions the influential turbulent structures within the SAF are now characterized.

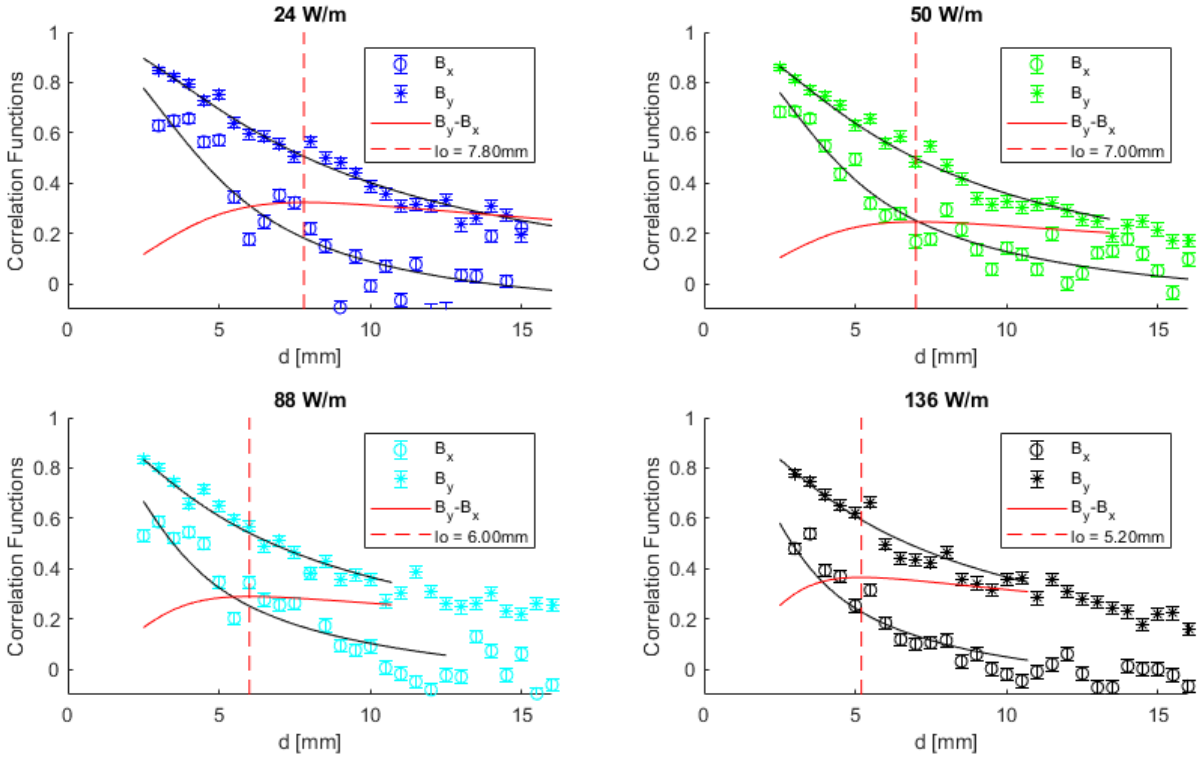

Figure 4.8: Correlation plots at various heat rope powers. The peak of the red solid line ($B_y - B_x$) is marked by the red dashed line. The x intercept of the red dashed line is the approximate l_o.

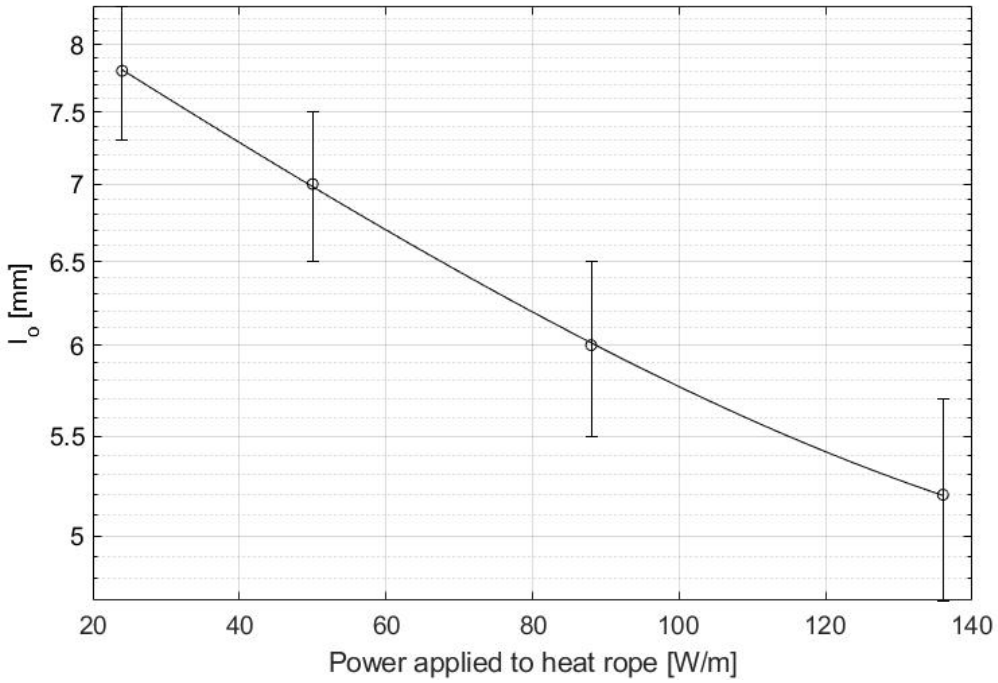

Figure 4.9: Estimate of inner length scale l_o at increasing heat rope powers. Error bars are representative of the discretization of step size between test cases, d.

5. TURBULENT INTENSITY: FILTERED RAYLEIGH SCATTERING

5.1 Background

This section describes the direct measurement of the turbulent intensity, parameterized by C_n^2, using light scattering diagnostics. Previous optical turbulent interaction studies have used constant current or temperature anemometers (CCA or CTA) to extract temperature structure constants [34]. Another alternative is to use scintillometers which rely on classical scaling laws for scintillation described in section 2. [15]. Both of these methods rely on presumptions about the turbulence environment. For the characterization of the the turbulence within the SAF, a novel approach was taken that utilizes Filtered Rayleigh Scattering (FRS). FRS is a non-intrusive flow diagnostic technique that can extract flow parameters such as density and temperature without requiring the use of a physical probe infringing on the flow field. In the following sections the refractive index structure constant and the motivation behind using FRS will be described in detail.

5.1.1 Refractive Index Structure Constant

The index of refraction, n, describes both the dispersive and dissipative effects of a medium on light propagation. Specifically, the real part conveys the effect of the medium on the phase speed while the imaginary component describes light attenuation. Here we focus on the phase speed, which is equal to $c/Re(n)$ in a medium with refractive index n.

The relationship between n and the medium density can be observed in the classical Lorentz model of neutral atom which is described by in the context of refraction by Feynman [35]. If one takes the applied field to be $E = E_o e^{iw(t-z/c)}$ through a medium of width z, the resulting electromagnetic field after the medium is then,

$$E_a = E_o e^{i\omega(t-z/c)} - \frac{i\omega(n-1)\Delta z}{c} E_o e^{i\omega(t-z/c)}, \tag{5.1}$$

where $\Delta t = (n-1)\Delta z/c$ due to the field produced by the charges. In the classical model,

the motion of an electron perturbed by an electromagnetic field is given by $x = \frac{q_e E_o}{m_e(w_o^2 - w)} e^{iwt}$. Using this expression and the assumption that the medium can be modeled as a sheet of charges in congruent motion, the electromagnetic wave dispersion as a function of material properties can then be represented as,

$$E_a = -\frac{\eta q_e}{2\epsilon_o c}\left[i\omega \frac{q_e E_o}{m_e(\omega_o^2 - \omega)} e^{i\omega(t - z/c)}\right]. \tag{5.2}$$

Setting equations 5.1 and 5.2 equivalent to each other and relating the number of atoms per unit area, η, to the number of atoms per unit volume, N the term Δz cancels and the final form of the index of refraction is then,

$$n = 1 + \frac{Ne^2}{2\epsilon_0 m_e(\omega_o^2 - \omega)}. \tag{5.3}$$

The expression for index of refraction in equation 5.3 gives insight into the mechanisms that influence the microscopic light matter interaction. Along with molecular species and electromagnetic wave dependencies, increasing the density of the species, N, also induces an increase in refraction. Equation 5.3 can be further simplified by using the Gladstone-Dale constant to estimate the effects from the electrons perturbed by the electromagnetic field.

$$n = 1 + K_{GD} N \tag{5.4}$$

The index of refraction is therefore directly related to the density of the medium, N.

Although, from an atmospheric optics perspective one is more interested in the spatial or temporal variation of n throughout the medium. If the entire medium contained a uniform density or index of refraction, a propagated beam's mean intensity profile would change but there would not be any variations or aberrations through time or space. If the entire medium was instead composed of a random distribution of refractive structures, as the atmosphere actually is, both the mean and fluctuation of the beam profile would be effected by propagation. This is of more interest at present, for it is the fluctuations in the electromagnetic waves that gives rise to scintillation. Therefore, in order to quantify this phenomenon, a metric for refractive index fluctuations needs to be introduced.

Deriving a quantity that tracks the spatially dependent fluctuation of refractive index begins with assuming n is a statistical function dependent on space ($\boldsymbol{r}$) and time (t), $n(\boldsymbol{r}, t)$. The refractive index structure function, C_n^2 is then introduced as a representation of the time averaged fluctuation magnitude of the refractive index between two points separated in space. This fluctuation is taken at two points $\boldsymbol{r_1} = \boldsymbol{r}$ and $\boldsymbol{r_2} = \boldsymbol{r} + \boldsymbol{x}$ that are separated by the vector $\boldsymbol{x}$. A pure Kolmogorov scaling for turbulence then yields a structure function [25],

$$\langle |n(\boldsymbol{r_1}) - n(\boldsymbol{r_2})|^2 \rangle = C_n^2 r^{2/3}. \tag{5.5}$$

Atmospheric models of C_n^2 have been created using empirical data to create a best fit ensemble average profile. These models predict that C_n^2 is typically on the order of 10^{-14} m$^{-2/3}$ near the surface of the Earth and 10^{-17} m$^{-2/3}$ at altitudes greater than 5 km [36]. Figure 5.1 shows the commonly used Hufnagel-Valley 5/7 C_n^2 model. This model is used as a best estimate of C_n^2 for preliminary AO device design. Although it has been found that C_n^2 can vary drastically due to environmental conditions, the HF-5/7 is an acceptable order of magnitude estimate. Using the data shown in figure 5.1 will prove useful for validating the experimentally determined C_n^2 within the SAF.

To experimentally determine C_n^2, $n(\boldsymbol{r}, t)$ or its proxy, density, must be measured within the medium of propagation. For SAF characterization this entails a spatial and temporal density measurement of the turbulent field produced by the heat rope. This density distribution can then be input into equation 5.4 to calculate $n(\boldsymbol{r_1}, t)$ and $n(\boldsymbol{r_2}, t)$. Using this conversion, equation 5.5 can then return a value of C_n^2.

When using a CTA or CCA for calculating C_n^2, one first assumes Taylor's frozen flow hypothesis, which uses the bulk flow speed to relate spatial and temporal measurements at a single location in space [37]. That is, knowing the bulk flow speed one can convert a temporal measurement into a spatial measurement by assuming the eddies are convecting across the probe location without distorting [34]. As previously stated, the characterization of the SAF was intended to minimize

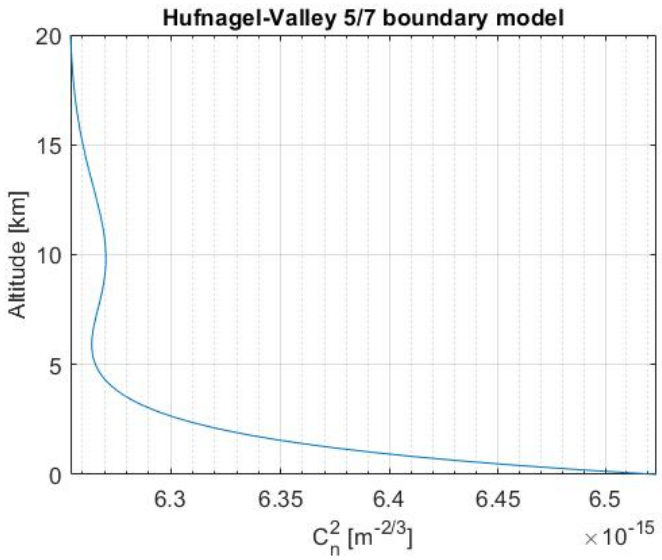

Figure 5.1: Hufnagel-Valley 5/7 theoretical model of C_n^2 [1].

the appeal to assumptions, therefore the Taylor's frozen hypothesis was deemed inadequate for the experimental procedure. This motivated the use of Filtered Rayleigh Scattering. This technique allowed for the measurement of the density along a 120 mm line segment of turbulence produced by the heat rope at a rate of 30 recordings per second, the repetition rate of available laser systems. Thus, providing a calculation method for $n(\boldsymbol{r}, t)$ without invoking Taylor's hypothesis.

5.1.2 Filtered Rayleigh Scattering

In order to understand the motivation behind using the Filtered Rayleigh Scattering (FRS) diagnostic technique within the SAF, a brief outline of the mechanisms behind FRS will be presented. The purpose of this brief derivation is meant to arrive at key dependencies in the scope of the SAF characterization. For a more in depth explanation of FRS refer to Miles' article [38].

Primarily, Rayleigh scattering is a regime of light scattering from molecular or atomic excitation[39]. This scattering is induced by creating a dipole moment ($\boldsymbol{p}(t)$) brought about by the acceleration of electrons bound to an atom. What differentiates Rayleigh scattering from Mie (particulate) scattering, is that for Rayleigh scattering to occur the diameter of the molecule or atom must be smaller than the wavelength of light ($\lambda >> d_a$). With this assumption, the spatial distribution of the photon

induced polarization can be ignored and the driving force of the electron is given by $-eE_o e^{-i\omega t}$ for a harmonic field.

Using this driving force from the electromagnetic wave, the dipole moment can be modeled using the Lorentz oscillator model as,

$$\boldsymbol{p}(t) = \frac{e^2/m_e \boldsymbol{E}(t)}{\omega_0^2 - \omega^2 - i\gamma_l t}. \tag{5.6}$$

γ_l is the dissipation coefficient of the oscillator. For FRS experiments it is of interest to define the ratio of the radiated power caused by the scattering per solid angle ($\frac{dP_s}{d\Omega}$) to the applied excitation intensity (I_{laser}) of the laser light. This metric can then be captured with an imaging camera during experimentation. The derivation of the scattered power begins by determining the differential Rayleigh scattering cross-section for a spherically symmetric scatterer[38],

$$\sigma'_{ss} = \frac{dP_s}{d\Omega}\frac{1}{I_{laser}} = \frac{e^2/m_e}{4\pi\epsilon_o(w_o^2 - w^2 - i\gamma_l t)} k^4 sin^2(\theta) = \alpha_v^2 k^4 sin^2(\theta). \tag{5.7}$$

Integrating σ'_{ss} over 4π steradians, the total Rayleigh cross section is returned,

$$\sigma_{ss} = \frac{8\pi}{3}\alpha_v^2 k^4. \tag{5.8}$$

In experiments, the intensity of the scattered light (I_R) can be described using knowledge of the differential Rayleigh cross section and experimental parameters.

$$I_R = I_{laser} N \Omega l \epsilon \frac{d\sigma_{ss}}{d\Omega} \tag{5.9}$$

The terms in equation 5.9 are shown graphically in figure 5.2. The solid angle is denoted by Ω, the efficiency by ϵ, and the length of the probe volume l. All of these terms are dependent on the experimental setup or environment.

The proportionality between the intensity at a point in the medium in which the temperature is

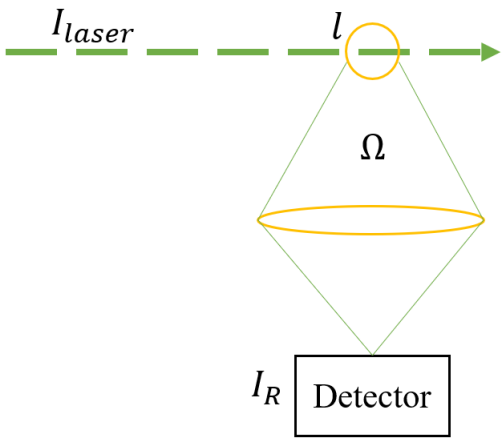

Figure 5.2: Explanation of the dependencies of experimental parameters on Rayleigh scattering intensity.

known (A) can then be compared to the intensity of a point of unknown temperature (B) [38]. If all experimental parameters are held constant the only term in equation 5.9 that remains after dividing the intensities are the respective densities N_A and N_B.

$$\frac{I_{R,A}}{I_{R,B}} \propto \frac{N_A}{N_B} \tag{5.10}$$

Then by invoking the the ideal gas law,

$$N = \frac{pA_o}{RT} \tag{5.11}$$

the intensity of the perturbed beam can be related to temperature fluctuations,

$$I_R \propto N, \quad I_R \propto \frac{1}{T}. \tag{5.12}$$

In an ideal scenario, the intensity of the Rayleigh scattering from an unperturbed flow field at a constant temperature (ambient conditions) could be compared to a perturbed field under the same experimental conditions. The intensity variation between the two tests could then be connected to temperature measurement of the unknown field using equation 5.10. Although, in an actual

experimental setting, usable results from a Rayleigh scattering measurement is often unattainable. Light reflections off of optical components or particulate (Mie) scattering often dominates the faint intensity created by Rayleigh scattering. To mitigate the effects of adverse testing conditions an alternative Filtered Rayleigh Scattering approach can be taken.

FRS uses the same principle as Rayleigh scattering in that the ratio between perturbed and unperturbed flow fields are used to extract useful parameters. The difference is that the favorable and unfavorable light are first passed through a molecular absorption filter before collection on the detector [38].

The frequency of the Rayleigh scattered light is broadened in comparison to the excitation laser. Light from reflections and particulate scattering are more intense, but are of a wavelength at or very close to the wavelength of the excitation laser. Therefore, if a narrow wavelength filter is set to approximately the same wavelength as the excitation laser, the unfavorable light will be blocked while the broadened Rayleigh scattered light is transmitted through to the intensity detector.

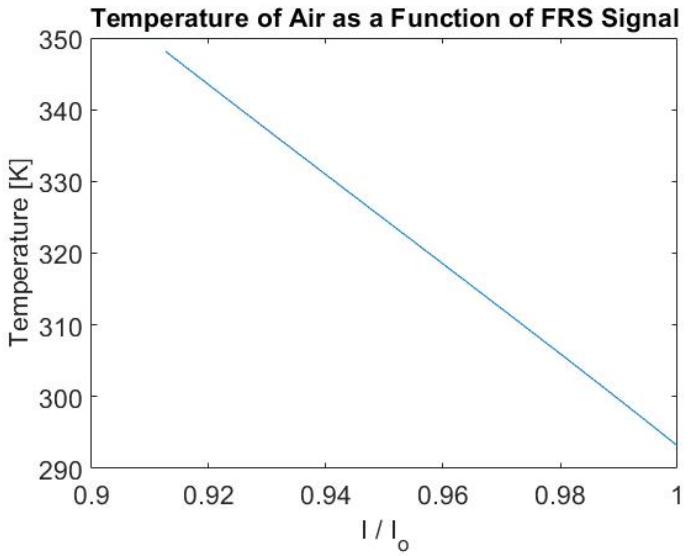

Figure 5.3: Model results of air temperature as a function of FRS transmission signal.

The FRS method uses a molecular absorption filter to block out the unwanted light. Various

molecules can be used for absorbing stray light. The choice of the molecular filter is made based off of the wavelength of the excitation laser in comparison to the absorption spectrum of the molecule. In this experiment a frequency doubled (532 nm) Nd:YAG laser was readily available. Therefore, Iodine (I_2) was used due to this molecules dominant absorption features around 532 nm [40]. The amount of broadened light that has leaked through the iodine filter needs to be connected to a temperature measurement in post processing. This is achieved using models of the Rayleigh scattering lineshape and I_2 absorption. Primarily, a MATLAB simulation of the absorption spectrum of gaseous iodine developed by Joseph Forkey specifically for Nd:YAG wavelengths was used [41]. This model returns the absorption of Iodine based off of the temperature and number density of the cell. Furthermore, a MATLAB version of the S7 code for Rayleigh Brillouin Scattering created at Princeton [42] was used for the scattering line shape. The resulting Iodine absorption spectrum and Rayleigh scattering lineshape from the simulation code can be seen in figure 5.4. Due to the Rayleigh line shape's is dependence on the temperature of the field the exact temperature of the flow can be computed by measuring how much light was transmitted through the filter and comparing it to the models. Figure 5.3 plots the intensity ratio from equation 5.10 to the temperature of the flow using the Forkey code. The density of the flow is returned as a function of temperature by means of the ideal gas law. This results in a measurement of the density distribution within the turbulent flow field.

5.2 Filtered Rayleigh Scattering: Experiment

Performing a FRS analysis requires specific hardware to stimulate, filter, and collect the scattering light from the air molecules within a field of interest. To begin the experimental setup, an adequate scattering excitation laser is required. A Q-swtich triggered Nd:YAG Continuum 30 Hz pulsed frequency doubled 532nm laser was used for this experiment (Continuum, Milpitas, CA) due to this laser's consistent Gaussian beam profile, high power per pulse, and ability to be injection locked. Rayleigh scattering is proportional to the amount of energy injected into the medium. Thus, a higher powered laser results in a greater signal of density fluctuations. Along with intensity, a stable wavelength of the laser is required to lock on to the absorption spectrum

of the molecular filter. To lock the Nd:YAG laser wavelength, a tunable ThorLabs diode laser was used to injection seed the higher powered system (12 W Laser Diode Temperature Controller, ThorLabs, Newton, NJ). The TEC was set to lock the Nd:YAG to the absorption feature shown in figure 5.4. The locked to absorption feature was chosen because of the feature's large spectral thickness in comparison to the broadness of the Mie scattering. A thick feature helps mitigate slight wavelength drift from affecting data collection. After splitting the TEC laser, one portion of was fed into the Continuum system for locking. The other portion of the TEC laser was directed into a WS7-60 Wavelength Meter (HighFinesse, Graefelfing, Munich) to monitor the wavelength the laser was tuned to during test. This wavelength meter is capable of measuring the wavelength within 60MHz accuracy at a 500Hz update speed. This error is acceptable for the experiment due to the thickness of the chosen iodine absorption feature. It was found that after the Nd:YAG laser and TEC reached thermal equilibrium there was very little drift in the wavelength through time. The laser is then imaged with a high sensitivity camera triggered at the same time as the laser pulse.

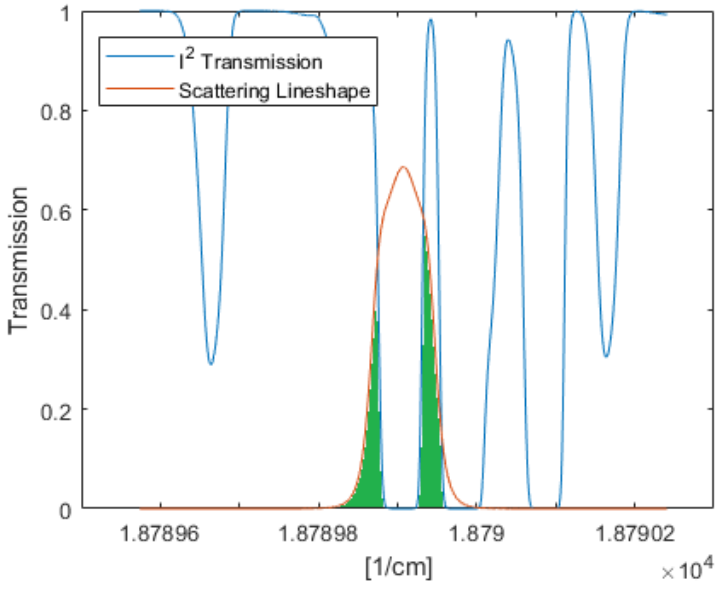

Figure 5.4: Absorption spectrum for Iodine at test conditions overlaid with Rayleigh scattering lineshape.

The synchronization of imaging with the laser pulse keeps light from ambient light sources and reflections off distant optics to a minimum. The imaging system chosen for this experiment was an ICCD PIMAX 532nm sensitive gated camera (Teledyne Princeton Insturments,Thousand Oaks, CA). This camera is capable of applying an emICCD gain to the incoming light. An emICCD gain allows for low light collection, linear gain to intensity mapping, and the ability to reach high rates of collection even with the gain activated.

The final piece to the FRS experimental setup is the Mie scattering molecular filter. For this experiment a molecular iodine vapor reference cell from ISSI was used (ISSI I2M-5, Innovative Scientific Solutions Inc., Dayton, Ohio). The cell was placed in between the field of interest and the camera to absorb the light before imaging. The properties of the iodine vapor must be held constant so that the molecular absorption features do not vary from shot to shot. To help with maintaining conditions this particular iodine cell is starved of particles. Starving the cell limits the number of iodine particles absorbing the laser light. This creates an upper limit to absorption at higher temperatures. The temperature of the cell was held constant with a proportional, integral, and derivative closed loop controller outfitted with a K type thermocouple jack (Digi-Sense Benchtop PID Temperature Controller, Cole Parmer, Vernon Hills, IL). This controller maintained the state of the molecular absorption feature throughout experimentation.

Refer to figure 5.5 for a component level breakdown of the the experimental layout. Due to the cumbersome experimental equipment and optical path lengths required, the FRS test could not be conducted within the SAF tubes. Although, the same heat ropes and power supplies as the ones in the SAF were used to generate a similar buoyancy driven turbulent plume in open air. Care was taken to not place any equipment within a 2 ft radius of the heat rope in order to not induce interaction with the plume not seen in the actual SAF. The heat ropes were mounted on a movable chassis while the imaged laser line was held at a constant height. An image of the experimental layout can be seen in figure 5.6, and in which, the adjustable heat rope is labeled. With this setup, the camera only needed to be focused once to the field of interest. By incrementally moving the heat rope further from the laser line, a 2D cross section of the turbulent plume was measured. The

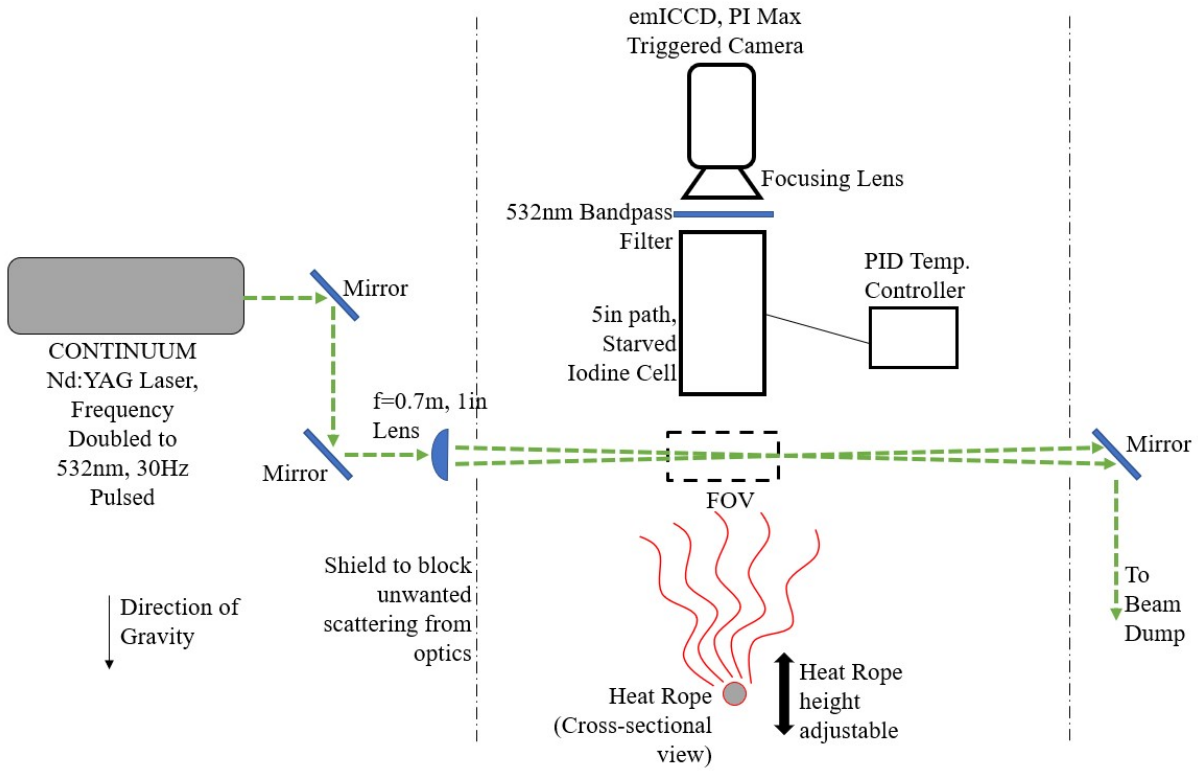

Figure 5.5: Optical and hardware component schematic for the FRS experiment conducted outside of the SAF.

laser was focused using a 0.7 m focal length lens. Due to particles in the air crossing through the focal point of this high powered laser, occasional plasma breakdown would occur. The intense flash caused by the plasma could saturate the camera causing possible damage to the sensitive photodetector chip. Therefore, the camera was focused slightly offset from the focal point (shown in figure 5.5). Due to the large focal length of the focusing lens, the beam waist was still much smaller then the expected smallest turbulent length scale even at this defocused region. The field of view scale can be seen in figure 5.8. A 532nm bandpass filter was placed between the camera and iodine cell to further help block stray light. To complete the experimental setup, black painted shields were setup to block laser light reflecting off of optical elements from being detected by the camera.

Tests were conducted at heat rope to laser line distances varying from 0.5 in to 6.0 in at 0.5 in increments to compare the difference in temperature fluctuations as the plume mixed with larger

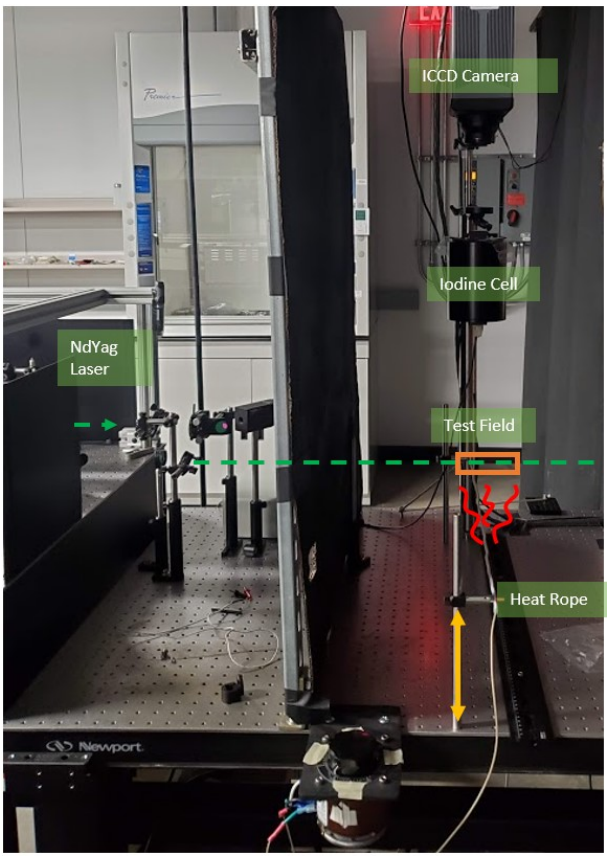

Figure 5.6: Experimental setup of FRS heat rope study. Components are labeled. The heat rope height is adjustable along the direction of the yellow arrow.

amounts of ambient air. The set points of the power supplied to the heat rope was kept similar to the parallel beam correlation experiment and Schlieren imaging at 24, 50, 88, and 136 W/m. This allowed for a direct comparison to the other characterization tests.

As mentioned in the section 5.1.2, an unperturbed reference field needs to be imaged for comparison to the perturbed field. Therefore, to begin each test at a heat rope to laser line distance, the heat rope was powered off and a series of images were collected with the laser tuned to the iodine absorption feature. This reference field contained the exact experimental conditions as the aberrated tests to come including reflections off of surfaces and Rayleigh scattering due to the ambient conditions of the air. To collect the Rayleigh scattering from the perturbed field the heat rope was first powered on to the first power set point, allowed to reach steady state, the tuned laser was fired,

and then a series of images were collected. The heat rope power was then increased, once again allowed to reach steady state, and the laser line was imaged. This procedure was repeated until all designated heat rope power set points and heat rope to laser line distances were collected.

5.3 Post Processing

In order to return the temperature field from Rayleigh scattering, an average reference field, I_{ref}, and a perturbed field, I, void of all particulate scattering and hardware induced shot noise are needed. The ratio between the two fields can be calculated to find the FRS signal. This signal is then input into the model shown in 5.3 to return the final temperature at each pixel.

To begin the post processing, an average of multiple images were taken with the laser turned off. Subtracting this average noise field, $\langle I_n \rangle$, from each successive image during experimentation will help increase sensitivity to the FRS signal. The following relationship was used to find the FRS signal at each time step, $I_r(t)$ [43],

$$I_r(t) = \frac{I(t) - \langle I_n \rangle}{\langle I_{ref} - \langle I_n \rangle \rangle} \tag{5.13}$$

Angle brackets denote temporal averages. The average of the reference images is denoted as $\langle I_{ref} \rangle$. By inspection of equation 5.13, a statistical average of the intensity field as well as a single instance of the intensity field in time are both necessary for temporal resolution of the fluctuating field. Non-ideal experimental conditions were found to be affecting the recording of I and $\langle I_{ref} \rangle$. Therefore, the procedure for temperature computation was less straightforward than just applying equation 5.13. The post processing method laid out in the following section was created to mitigate many of these experimental issues without compromising the accuracy of results and conclusions.

It was found that during experimentation a portion of the Mie scattering was not totally absorbed by the iodine filter. Shown in the uppermost image of figure 5.7 is a single shot of the camera. Notice the spikes in intensity pointed out in the image. The spikes denote locations in which the Mie scattering leaked through the filter. The middle image of figure 5.7 shows the result of averaging over all of the data set with the hope of getting rid of unwanted spikes. While the field

does seem much smoother, the excessive intensity of some Mie scattering spikes within the data set are still present in the mean field. The location of the bleed through is pointed out in the image b) of figure 5.7. Due to the inadequacy of simply taking a temporal average, an alternate method is needed to ignore these spikes in intensity and return a smooth averaged field for $\langle I_{ref} \rangle$. One algorithm to mitigate these adverse effects of Mie leak through is described by Limbach [43]. The first step of the algorithm is to calculate the temporal average and standard deviation at each pixel throughout the data set. This returns a spatially distributed averaged field with an associated range of acceptance at each location. The data set is then stepped back through and each individual pixel of each image is reassessed for scattering spikes. If the pixel's intensity value is outside a factor (A) of the standard deviation from the mean value at that pixel's location, then the tested pixel is omitted from the data as it is deemed an unwanted Mie scattering spike.

$$|I(x,t) - \langle I(x) \rangle| < A * std(I(x)), \quad KEEP \quad I(x,t) \tag{5.14}$$

$$|I(x,t) - \langle I(x) \rangle| > A * std(I(x)), \quad OMIT \quad I(x,t) \tag{5.15}$$

After recomputing the mean with the first round of exclusions not included, the procedure is then repeated, stepping back through all of the images until a successive iteration results in omitting no pixels. The lower image of figure 5.7 is the temporal average utilizing the Mie scattering omission algorithm. Notice how the faint spikes present in the middle field are no longer visible. Using this method an average of the irradiance field void of intensity spikes is returned which can be used as the term $\langle I_{ref} \rangle$ for calculating the FRS signal.

The next challenge is to find a method for computing a smooth intensity field of a single, non-averaged image of the aberrated field. This posed a major challenge once again due to the excessive amount of particulate scattering corrupting the FRS signal during experimentation. Many methods for single image smoothing were attempted such as spectral filtering, but after further consideration, temporal resolution of the temperature field was abandoned due to errant results. Turning back to averaging methods, the algorithm described above for finding $\langle I_{ref}(x) \rangle$ was also

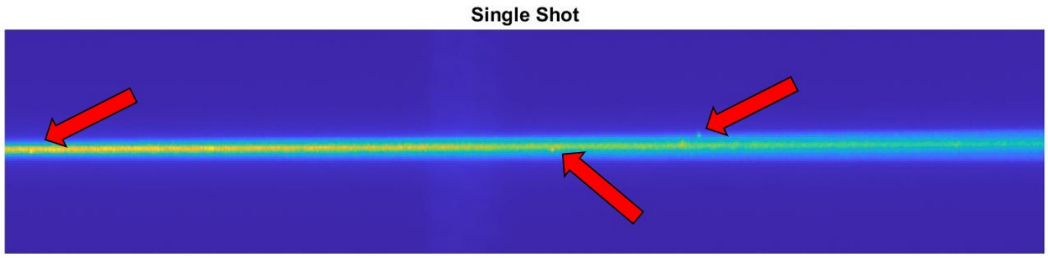

(a) Individual image with no averaging applied.

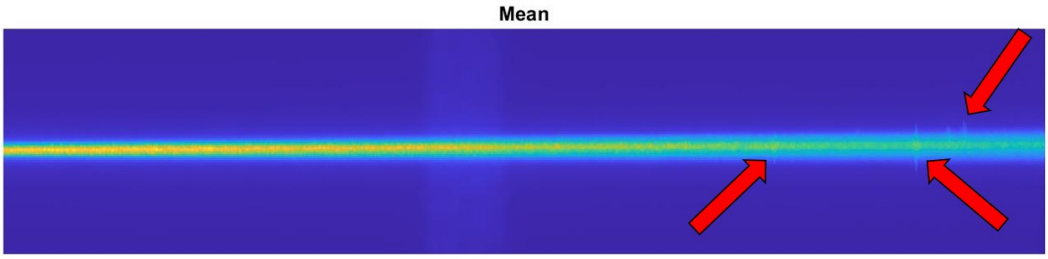

(b) Average beam intensity over a data set.

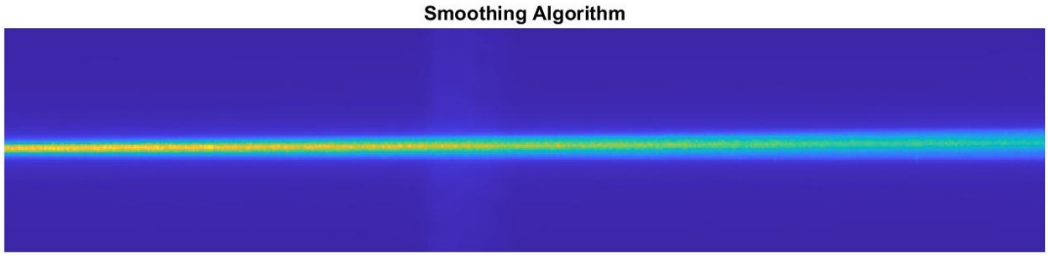

(c) Intensity field after the iterative smoothing algorithm is applied.

Figure 5.7: Progression of beam profile smoothing. Red arrows point out imperfections due to Mie scattering bleed through.

used for finding the irradiance ratio $\left\langle \frac{I(x)}{\langle I_{ref}(x) \rangle} \right\rangle$. Stepping through each image and omitting particulate scattering spikes, the mean and root mean square (RMS) of the smoothed irradiance ratio was computed. The average irradiance ratio was then input into the models developed by Forkey and Pan in order to return a spatial distribution of the average temperature profile. The results for a particular test scenario are shown in 5.8.

Notice how the temperature is greater at the location of the heat rope and then decays as the high temperature plume mixes with ambient air further out. Furthermore, the increased variance at the location of the heat rope indicates increased temperature fluctuation at this locations. In shot to shot images, the high temperature portion of the plume can be seen oscillating back and forth

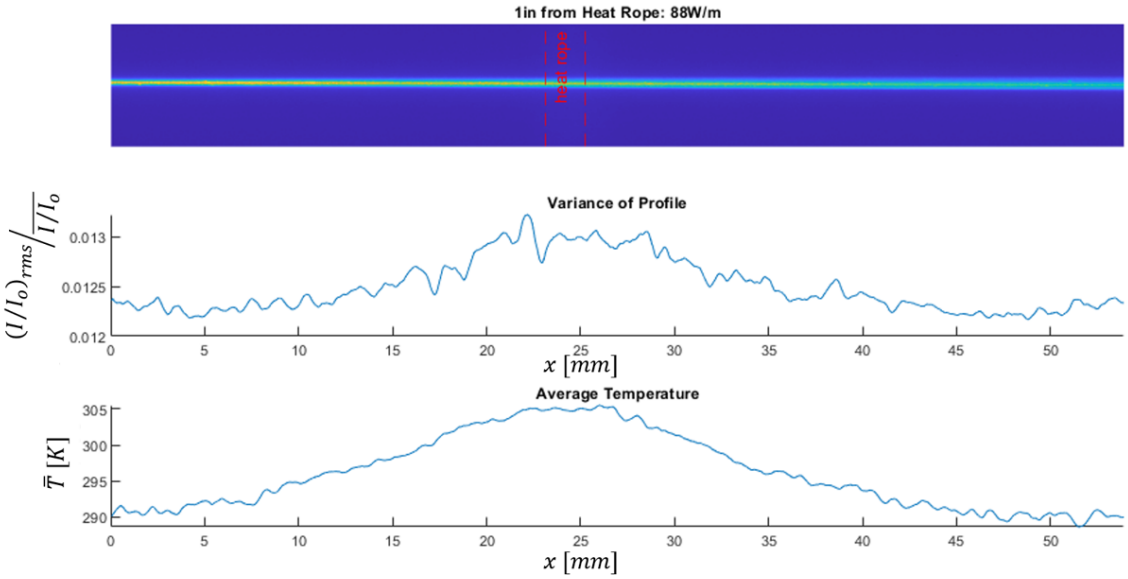

Figure 5.8: Uppermost image is a single shot capture of a beam profile. The middle plot is the spatial distribution of intensity variance. The bottom plot is the spatial distribution of the average temperature. Heat rope is located at approximately 25 mm in all plots.

with respect to the heat rope indicative of the recorded RMS fluctuation in figure 5.8. The variance does not fall off to zero outside of the plume ($x < 5mm$ or $x > 45mm$) due to the presence of experimental noise at these locations.

While these average statistics show that the FRS experiment is capturing the physics of the turbulent environment, a temporal resolution of the turbulent field cannot be computed by averaging successive images together. Referring to equation 5.5, a temporal and spatial resolution of refractive index is necessary for the classical calculation of C_n^2. Therefore, an alternate method for determining C_n^2 using average statistics is needed for this analysis.

In their recently published work, Kumari and Donzis describe a method to determine C_n^2 as a function of average density fluctuations $\langle \rho'^2 \rangle$ [10]. This method will now be used in place of the traditional C_n^2 definition shown in equation 5.5.

The derivation begins with the relationship for the refractive index structure function,

$$D_n(r) = C_n^2 r^{2/3}. \tag{5.16}$$

Then, D_n is normalized with $2\langle n'^2\rangle$ and r is normalized with the integral path length of the turbulent field, L_o,

$$\frac{D_n(r)}{2\langle n'^2\rangle} = \frac{C_n^2 L_o^{2/3}}{2\langle n'^2\rangle}\left(\frac{r}{L_o}\right)^{2/3}. \tag{5.17}$$

Next, referring back to the traditional expression of the refractive index structure function,

$$D_n(r) = \langle[n(x+r) - n(x)]\rangle^2 = \langle n(x+r)^2\rangle + \langle n(x)^2\rangle - 2\langle n(x+r)n(x)\rangle. \tag{5.18}$$

A handful of logical assumptions will now be made to simplify equation 5.18 starting with the assumption that the flow is homogeneous. As a result, the first two terms in equation 5.18 can be considered equivalent. Also, it will be assumed that $r \to \infty$. With this approximation $n(x+r)$ and $n(x)$ are uncorrelated due to the very large distance between the two points. These simplifications result in the equation 5.18 collapsing to,

$$D_n(r) = 2\langle n'^2\rangle. \tag{5.19}$$

The assumption that $r \to \infty$ is now relaxed to $r \approx L_o$. This is acceptable due to the definition of L_o being that the integral length is the distance at which two points in the turbulent field are no longer correlated. The rightmost term, $\left(\frac{r}{L_o}\right)^{2/3}$, in equation 5.17 then collapses to a constant of first order. This constant will be referred to as $C_n'^2$. The next step is to use the definition of the Gladstone-Dale constant in relation to the refractive index to relate the terms in equation 5.19 to density fluctuations.

$$\langle \rho'^2\rangle = \langle n'^2\rangle K_{GD}^2 \tag{5.20}$$

$$C_n^2 = \frac{C_n'^2\langle \rho'^2\rangle K_{GD}^2}{L_o^{2/3}} \tag{5.21}$$

Equation 5.21 can now be used to find an approximate C_n^2 at each test scenario by computing the average fluctuation of the density $\langle \rho'^2\rangle$ with the FRS data set. Furthermore, as can be seen in the mean profile in figure 5.8, not every pixel in the field of view is effected by the heat-rope.

Taking the unperturbed region into account when calculating the average density fluctuation would result in an undershoot of the actual fluctuation. To make sure this under prediction does not effect the results, the full width half maximum (FWHM) of the average temperature profile was first calculated to determine the region of the 2D line that was impacted by the heat rope. This window (shown in figure 5.9) denoted the range of pixels used in each image to compute $\langle \rho'^2 \rangle$.

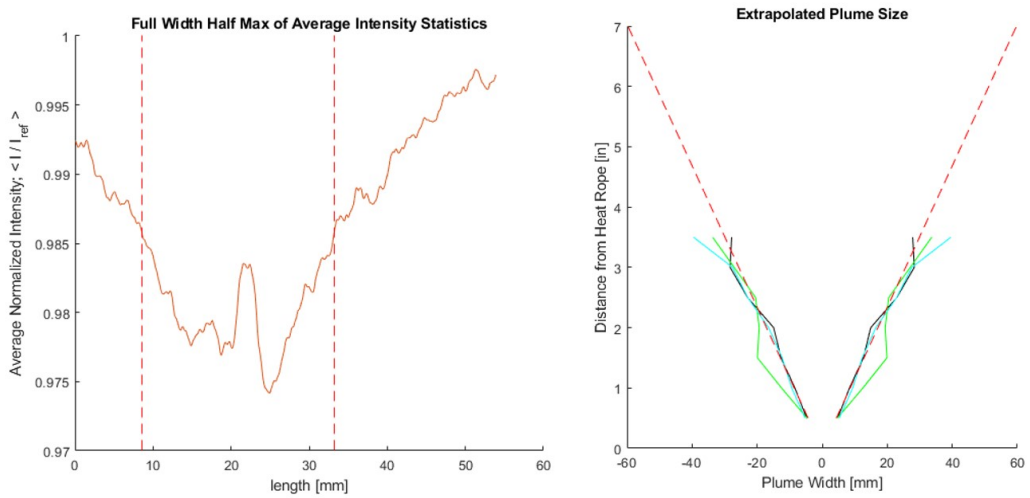

(a) FWHM calculation from an average intensity profile. (b) Extrapolation of turbulent plume width.

Figure 5.9: FWHM analysis of the turbulent plume average profiles.

With the introduction of the statistical estimate of C_n^2 the Gladstone-Dale Constant (K_{GD}^2) and integral length scale (L_o) now need to be derived. The Gladstone-Dale constant was found assuming standard atmosphere conditions, $K_{GD}^2 = (n_{air} - 1)/1.225[kg/m^3]$.

The integral length scale at the center line (7 in from heat rope to laser line) of the SAF is needed. L_o is the the largest turbulent structure within the flow. Therefore, L_o was taken to be the width of the diverging turbulent plume at the 7 in location. Using the same FWHM plume width method that was used to find the window of interest, the turbulent plume size was computed and then extrapolated out to the 7 in distance. The results of this procedure are shown in figure 5.9, concluding that $L_o \approx 120mm$ independent of heat rope power.

Distance [in]	24 W/m	50 W/m	88 W/m	136 W/m
0.5	0.0354	0.0560	0.0694	0.067
1.0	0.0181	0.0301	0.0492	0.0605
1.5	0.0171	0.0165	0.0367	0.0438
2.0	0.0090	0.0160	0.0208	0.0271
2.5	0.0082	0.0155	0.0184	0.0183
3.0	0.0095	0.0148	0.0159	0.0177
3.5	0.0101	0.0109	0.0155	0.0169
4.0		0.0106	0.0122	0.0115
4.5		0.0099	0.0117	0.0119
5.0		0.0072	0.0119	0.0127
5.5		0.0082	0.0114	0.0115
6.0		0.0091	0.0075	0.0109

Table 5.1: Table of averaged $\langle \rho'^2 \rangle$ FRS results at increasing heat rope power and distance.

The constant term of first order $C_n'^2$ is also unknown at this point. An estimate for this value will be found by comparing the FRS results to the characterization results from other experiments. The procedure for this derivation will be explained in the Results section 5.4.

The motivation behind the experimental layout and assumptions have now been explained. The results of using FRS to measure turbulent intensity can now be reported, using the estimation of C_n^2 by first measuring the average density fluctuations of the field.

5.4 Results

The following section will report on the concluded $\langle \rho'^2 \rangle$ at each test scenario. $\langle \rho'^2 \rangle$ was found at each testing scenario shown in table 5.1 using the noise mitigation and averaging techniques described in the Post Processing section.

Notice how the values of $\langle \rho'^2 \rangle$ become errant at larger heat rope distances. The FRS signal is too low at these larger distances to capture the smaller temperature fluctuations of the medium. To see this issue graphically, figure 5.10 shows averages and fluctuations of irradiance profiles of constant heat rope power at increasing heat rope distance. The turbulent statistical profiles at larger distances begin to flat-line, indicating that the signal is approaching the noise floor of the experiment causing the fluctuations in the field to become increasingly more difficult to detect.

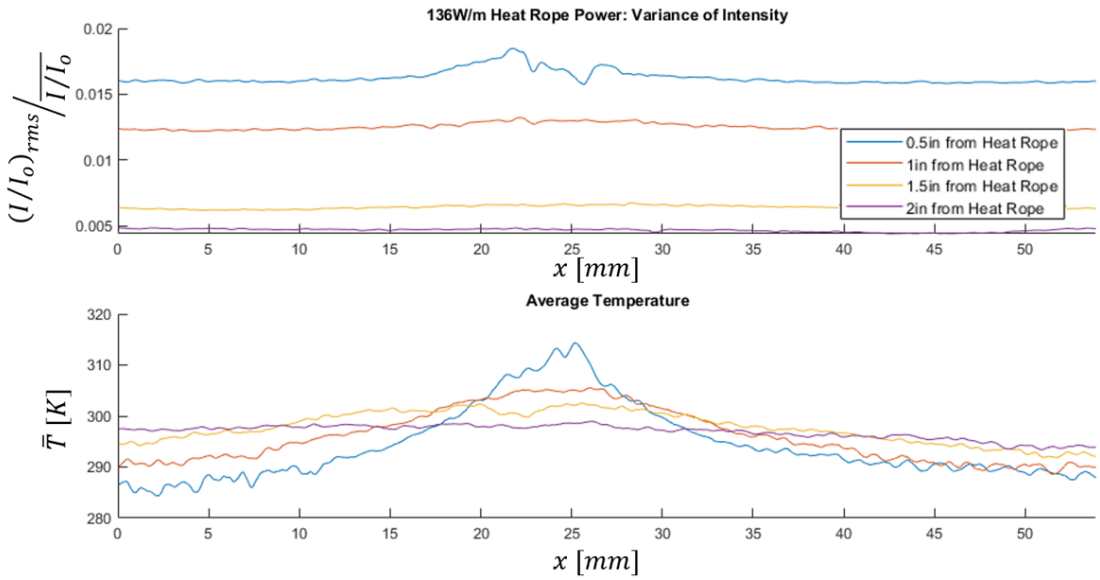

Figure 5.10: 2D turbulent field statistics using FRS. Upper plot is of the variance of intensity, the lower plot is of average temperature. The heat rope is located at approximately 25 mm.

The turbulent field statistics at the distance where the scintillation laser beam intersects the plume (7 in) is of the most interest. Although, the FRS measurement technique could only return usable measurements up to approximately 6 in from the heat rope (this distance varied for each heat rope power case). To solve this issue, the $\langle \rho'^2 \rangle$ data was first truncated at a distance prior to the signal collapsing to the noise floor. This truncated data set was then extrapolated out to the 7 in location.

Figure 5.11 shows the results at each heat rope power. The trend of the data agrees with what was expected. The increase in heat injection into the flow caused an increase in density fluctuations.

Now that the independent term $\langle \rho'^2 \rangle$ used within equation 5.21 is found experimentally, the final parameter to define is the constant $C_n'^2$. As previously mentioned and shown in figure 5.1, C_n^2 is a highly variable value within the atmosphere. Simply an order of magnitude estimate would be acceptable and usable in a characterization analysis. Therefore, an experimental error on the order of this first order term can be deemed acceptable. Although a value for $C_n'^2$ can still be arrived at in a logical manner. In order to maintain this characterization method's reliance on experimentation, the results from the scintillation and inner scale experiments will be used to find $C_n'^2$.

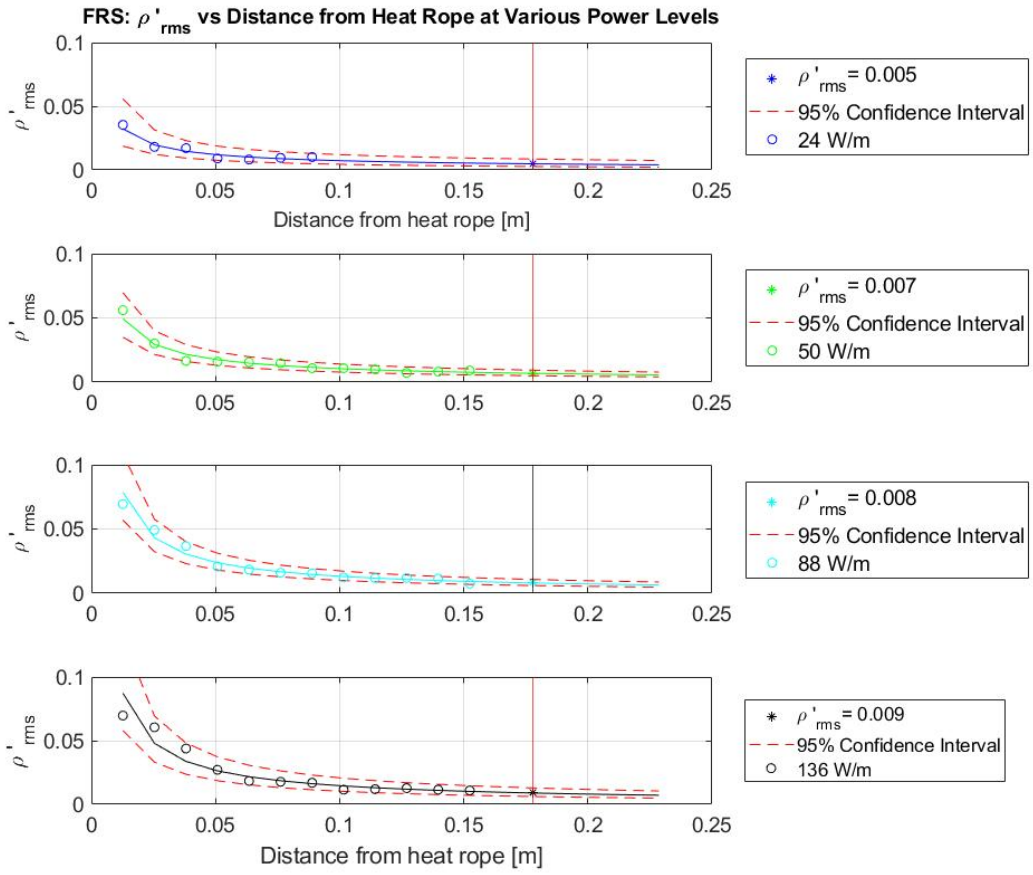

Figure 5.11: $\langle \rho'^2 \rangle$ profiles of the 2D turbulent field at various heat rope powers and distances from the heat rope. The degredation of FRS signal before 7 in of propagation was resolved by extrapolating the data using a least squares fit. A 95% confidence interval of the fit was also plotted to derive the C_n^2 calculation error.

It will be shown in chapter 6 that the SAF exists in the geometric optics regime (see figure 6.4). Therefore, the following theoretical approximation for scintillation shown in Lawrence's article [44] can be used to estimate σ_χ^2.

$$\sigma_\chi^2 = 12.8 C_n^2 L^3 l_o^{-7/3} \tag{5.22}$$

Using equation 5.22, σ_χ^2 can be found as a function of the experimentally determined parameters. This theoretical approximation can then be compared to the actually recorded scintillation data (this will be reported on in totality in chapter 6). The only variable in the approximation of

C_n^2 remaining is the value $C_n'^2$. Notice that C_n^2 in equation 5.21 is only dependent on the turbulent scale L_o , which was in turn determined to be independent of heat rope power (see figure 5.9). Therefore, $C_n'^2$ should be consistent in all of the test scenarios.

$$\sigma_\chi^2 = 12.8 \frac{C_n'^2 \langle \rho'^2 \rangle K_{GD}^2}{L_o^{2/3}} L^3 l_o^{-7/3} \tag{5.23}$$

Equation 5.23 can then be computed and compared to experimental data. The value of $C_n'^2$ resulting in the smallest difference between theory and experiment was found to be: $C_n'^2 = 6.0$. Figure 5.12 shows the comparison of an experimental scenario with the theoretical approximation using the converged upon value of $C_n'^2$.

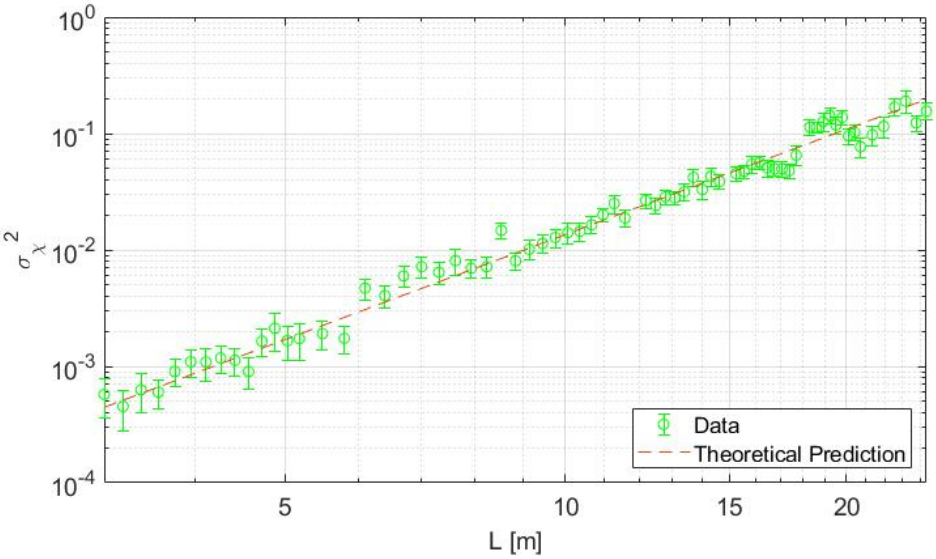

Figure 5.12: Theoretical comparison to data in order to define an acceptable value for $C_n'^2$.

All of the terms within equation 2.10 have now been independently measured. The magnitudes of C_n^2 found by equation 5.23 and using a value of $C_n'^2 = 6.0$ is reported in figure 5.13 and table 5.2 as a function of heat rope power. The error bars in the graph of figure 5.13 are obtained by solving for C_n^2 using the values of $\langle \rho'^2 \rangle$ that fall on the bounds of the 95% confidence interval shown in

figure 5.11.

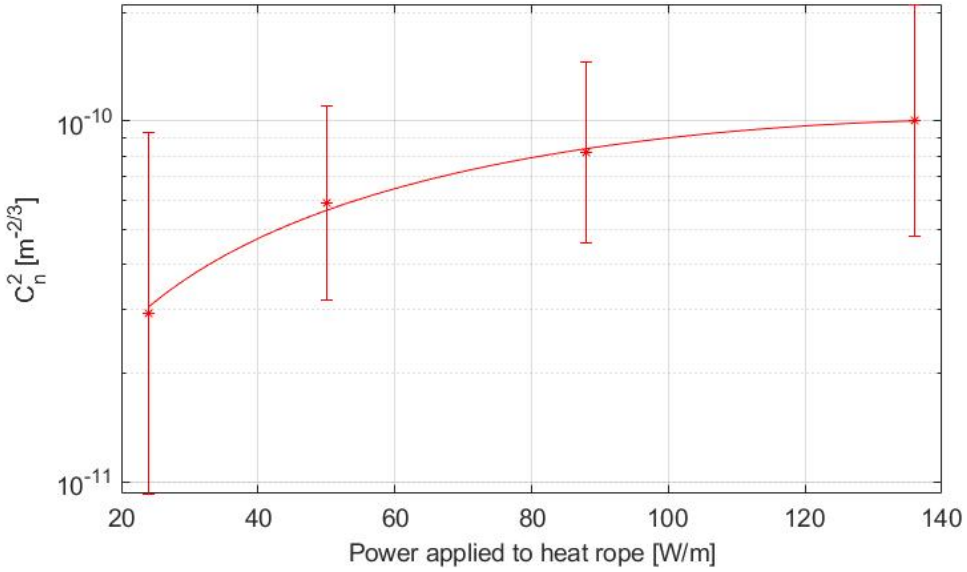

Figure 5.13: C_n^2 as a function of heat rope power.

Heat Rope Power [W/m]	$C_n^2[m^{-2/3}]$
24	$(2.93 \pm 2.00) \times 10^{-11}$
50	$(5.92 \pm 2.70) \times 10^{-11}$
88	$(8.18 \pm 3.60) \times 10^{-11}$
136	$(10.10 \pm 1.27) \times 10^{-11}$

Table 5.2: Tabulated C_n^2 values found using equation 5.21. Error was assigned using the 95% confidence interval of the $\langle \rho'^2 \rangle$ fit.

6. PATH LENGTH RESOLVED SCINTILLATION SCALING

6.1 Background

* The experiments up to this point have been focused on turbulent parameters used to predict atmospheric optic phenomenon, namely scintillation. To complete the study, the scintillation will now be explicitly measured within the SAF. The multiple access points along the SAF will be leveraged to complete a path length resolved data set of laser scintillation at various heat rope power settings.

The motivation behind an experiment of this type is rooted in the validation of scintillation scaling regimes. Foremost, the transitions between power scaling regimes (L^3 and $L^{11/6}$) is poorly understood in the literature today. It is common practice in testing facilities to assume that the beam under test is in the $L^{11/6}$ regime even at relatively short propagation distances [19]. This presumption would result in an under prediction of scintillation.The first transition occurs when the Fresnel number $F \approx 1$. At the propagation distance associated with a Fresnel number of unity, a path defined scintillation model may contain instabilities that do not agree with the actual scintillation scaling that occurs in nature [16]. Assuming a regime is also an issue with the usage of scintillometers. These devices rely on the approximation that $F > 1$, which might not be the case in low strength turbulence ($\sigma_c hi^2 << 1$) or at short propagation distances ($l_o^2/\lambda >> L$). A path length resolved scintillation experiment will allow for the detection of transitioning from one regime to another as well as track any instabilities that are not captured in theoretical models.

The definition of the distance dependent scaling will prove useful in characterizing the exact conditions that exist within the SAF. A well defined path length resolved scintillation measurement will lead to a source of experimental validation for the previously defined turbulent parameters as well as a comparison to theory.

A model to track fluctuations of intensity caused by the influence of turbulence in experimen-

*Part of this chapter is reprinted with permission "Laser Scintillation Measurement in a Controlled Turbulent Environment" by Grant Erickson, James Creel, Richard B. Miles and Christopher Limbach, 2022. AIAA 2022-0985 Session: Aero-Optics and Atmospheric Optical Turbulence Published Online:29 Dec 2021.

tation will now be proposed. This model will show the correct statistical parameter to compute in order to track the intensity fluctuations. Primarily, the beam will first be modeled using the Rytov approximation of an electromagnetic field, E [45] [46].

$$E = E_o exp(\psi) \tag{6.1}$$

The exponential term ψ tracks the oscillations of the beam about the mean E_o. This fluctuating term can be decomposed into an intensity component, χ, and a phase component, ϕ [].

$$\psi = \psi_1 + \psi_2 + ... + \psi_n \tag{6.2}$$

$$\psi_n = \chi_n + i\phi_n \tag{6.3}$$

Because this study is only interested in intensity fluctuations, the phase perturbation denoted by ϕ_n is neglected. Shown in equation 6.2 the exponential term can be expanded to infinite terms, n. Although only the first 2 orders of amplitude fluctuations, $\chi_{1,2}$, will be analyzed. Higher order terms are considered to be much smaller than these first two terms and are most likely within the noise floor of the detection apparatus. The beam equation under investigation is then collapsed by computing the amplitude and neglecting higher order terms of fluctuation.

$$I = |E|^2 \tag{6.4}$$

$$I = I_o exp(2\chi_1 + 2\chi_2) = [I_o exp(2\chi_1)]\, exp(2\chi_2) \tag{6.5}$$

If only the fist order log amplitude, χ_1, is solved for, then the distribution is clearly log-normal,

$$\chi_1 = \frac{1}{2} ln(I/I_o) \tag{6.6}$$

By including the second order term χ_2 the simplified log-normal distribution of intensity only including the first order approximation breaks down [46]. This fluctuating term χ_2 is what is

of interest. The traditional method to track the second order fluctuation term is to calculate the variation of the first χ_1 term. The log amplitude variance of intensity is commonly referenced using the symbol σ_χ^2 [16]. This statistic σ_χ^2 tracks the fluctuation of the second order term in precisely the manner desired [24].

$$\sigma_\chi^2 = \langle \chi_1^2 \rangle - \langle \chi_1 \rangle^2 \tag{6.7}$$

The log amplitude fluctuation σ_χ^2 will be used for comparison to other turbulent parameters. Although, other statistical moments of the log amplitude also give insight into the characteristics of the interaction phenomenon. The first 3 cumulents of the log-amplitude are used to give sufficient information about the probability distribution function (PDF) of intensity measurements. The cumulents are calculated as follows [46].

$$K_1 = \langle \chi \rangle \tag{6.8}$$

$$K_2 = \langle \chi^2 \rangle - \langle \chi \rangle^2 \tag{6.9}$$

$$K_3 = \langle \chi^3 \rangle - 3\langle \chi \rangle \langle \chi^2 \rangle + 2\langle \chi^3 \rangle \tag{6.10}$$

K_1 is the mean of the distribution. K_2 is a measure of the variation from the mean of the data set. K_2 is analogous with σ_χ^2. The final cumulent, K_3, tracks the skewness of the PDF. As turbulence increases in intensity or propagation distance gets large, the PDF of the intensity will likely become more skewed. In analyzing the K_3 cumulent as a function of intensity and distance, the increase in magnitude will denote a departure of the PDF from a LN distribution.

The skewness of the intensity can be seen in the image of the beam shown in figure 2.2. At shorter propagation distances the intensity pattern of the beam is more uniform with only slight variations in intensity. As the beam travels through more turbulence, thin striations of focused light begin to form. These high intensity striations in the profile are broken up by larger areas of lower beam intensity. As the fluctuations convect over the collection aperture in time, the larger low intensity portions are more prevalent. This leads to a logarithmic skewed distribution towards

the lower intensity values.

6.2 Experiment

The laser used in the scintillation experiment is a 18W Verdi Continuous Wave 532nm laser (Coherent Inc., Santa Clara, CA) and was positioned at the head of the SAF. The Gaussian intensity profile of the beam is expanded and collimated to a 4 in diameter. The beam is then propagated down the center of the SAF, 7 in above the heat ropes and directly down the center line of the tubes. This beam location was validated in the Schlieren experiment described in chapter 2. The full opto-mechanical setup is shown in figure 6.2 . During preliminary testing, spherically cut lenses were used for the expanding and collimating elements. It was found that the aberrations induced by these imperfect optics caused the beam profile to be unacceptable at propagation distances greater than approximately 30 ft. Therefore, aspherically cut lenses were used in the place of these two optics. This substitution improved the beam quality considerably.

At the location of beam intensity collection, a $400\mu m$ multi-mode fiber optic cable was attached to a mount and aligned with the center of the beam profile. A small collection aperture minimizes the averaging of intensity fluctuations [47],

$$\sigma_I^2 = A[exp(4\sigma_\chi^2) - 1] \tag{6.11}$$

If $\sigma_\chi^2 << 1$,

$$\sigma_I^2 \approx 4\sigma_\chi^2 \tag{6.12}$$

$$A = \left[1 + 1.07\left(\frac{kD^2}{4L}\right)^{7/6}\right]^{-1} \tag{6.13}$$

Equations 6.11 and 6.13 above were reported in [1] in reference to the aperture averaging coefficient, A, developed by Churnside [48]. In equation 6.13, D represents the diameter of the collection apertures. As D increases with respect to propagation distance, L, the coefficient A decreases. For the $400\mu m$ diameter optical fiber at maximum L, the coefficient $A = 0.99$. Therefore equation 6.12 is an acceptable approximation in substitute of equation 6.11. Also, aligning the small col-

lection fiber at the center of the gradually sloping 4 in diameter Gaussian beam allows for the approximation that the fiber is seeing a planar wave. The only intensity variation detected by the fiber is from the turbulence induced scintillation and not the decaying of the beam profile.

The fiber probe collects and transmits the intensity fluctuations back to a channel of a 2-channel balanced photo detector (PDB210A ThorLabs, 1MHz, Fixed Gain, Large Area Balanced Photodetector, Si PIN Photodiodes, Newton, NJ). The other channel of the photo detector is populated with a picked off, unperturbed portion of the beam. The photo detector computes a difference between the two intensity inputs internally and outputs an analog signal varying from +/-5V corresponding to the intensity fluctuation. The analog difference reduces the noise of the intensity fluctuation. The output from each channel as well as the difference is then logged onto a computer using a NI DAQx (National Instruments, Austin, Texas). Figure 6.1 shows the raw output signal for a given test case overlaid with a normalized value of the difference signal ($I_{Normalized}$). It can be seen that the high frequency noise caused by experimental error is greatly reduced in the normalization of the internally computed difference.

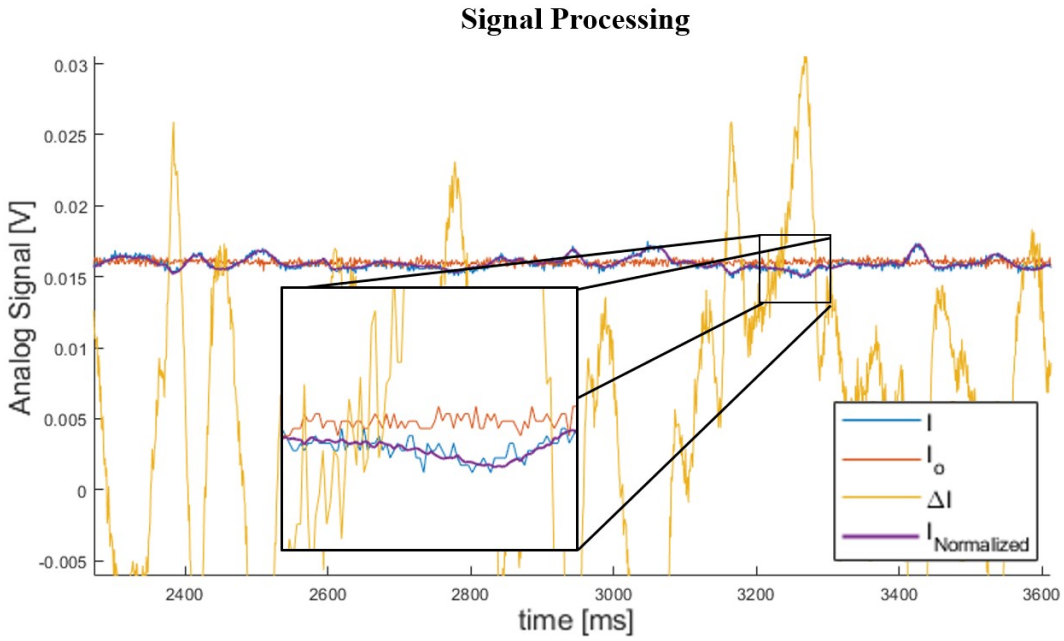

Figure 6.1: Raw signals from the 2 channel photodetector overlaid with the noise reduced and scaled version of the fiber signal ($I_{Normalized}$).

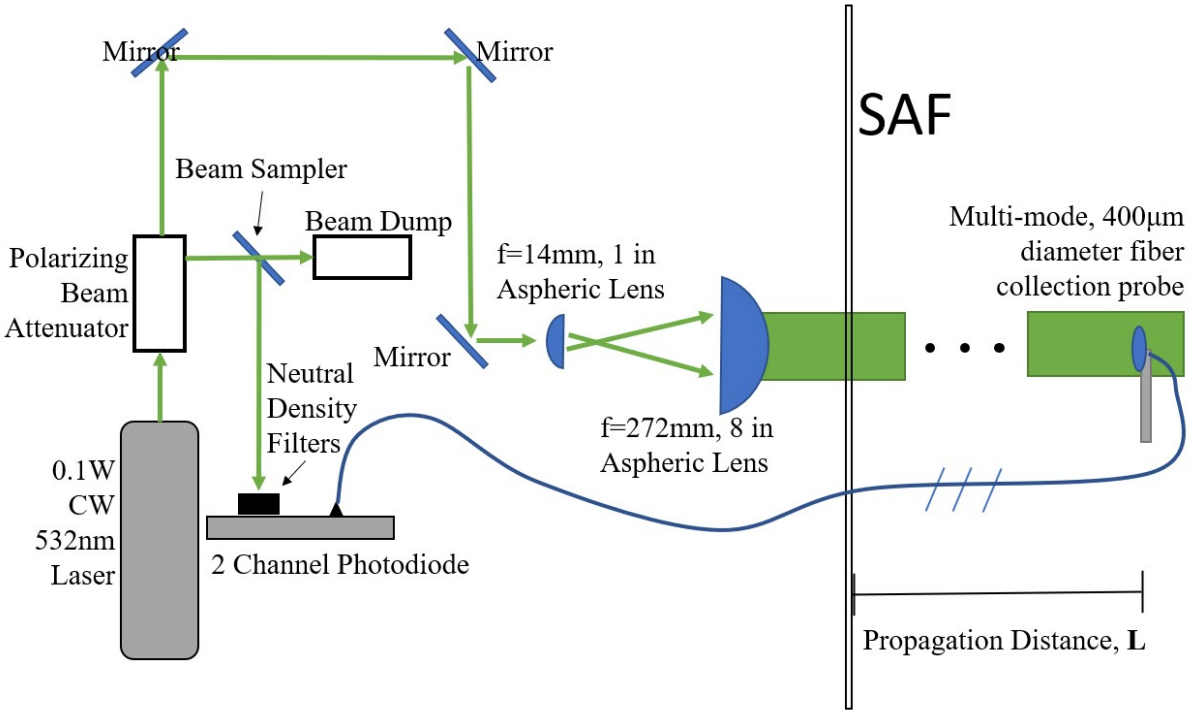

Figure 6.2: Optical components for scintillation test.

Using the apparatus shown in figure 6.3, the scintillation probe was stepped through the SAF to collect scintillation measurements. Due to the logarithmic scaling of $_2$ vs. L predicted in equation 2.11 the closer propagation distances require a step size smaller than that of the further distances. At distances < 10 ft the rig was stepped at 6 in increments; at intermediate distances $10ft < L < 70ft$, 1 ft increments were made; and at the furthest distances $70ft < L < 80ft$, 2 ft increments were made. The scintillation rig maintained the cross-sectional, x and y location of the fiber optic probe for any propagation distance L. Using the rig ensured that the probe encountered the same turbulent path characteristics at each propagation distance. Furthermore, at each distance L data was collected at heat rope powers of 6, 24, 50, 88, and 136 W/m. Referring to equation 2.10 and the results from previous experiments an increased heat rope power should increase scintillation.

At each distance and power setting, 5 minutes of data collection was taken at a collection rate of 1000 samples per second. It was found that 5 minutes (3e5 data points) of collection resulted in very well defined PDF's of the intensity data. Furthermore, the polarizing beam splitter as well

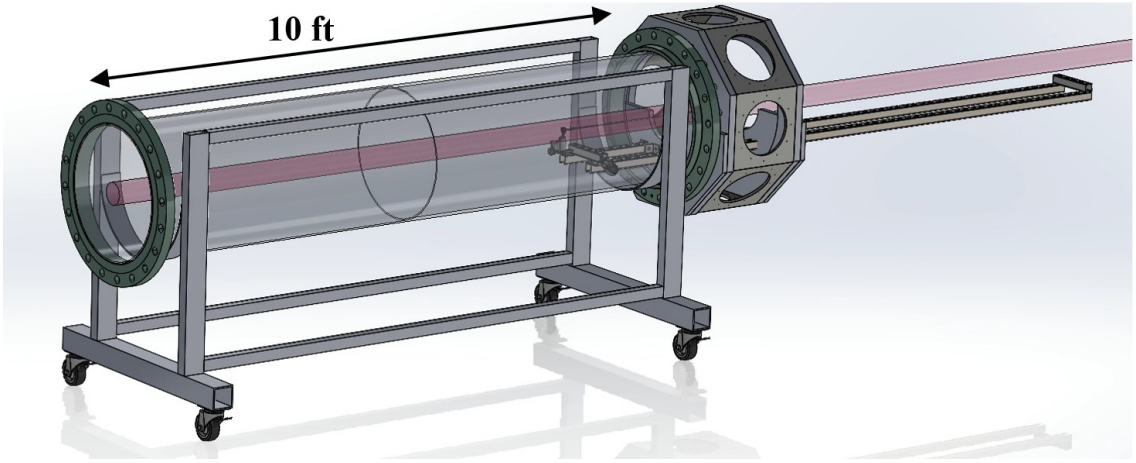

Figure 6.3: Model of scintillation rig built for the SAF. The rig allowed for the optical fiber probe to be inserted into the tube to record scintillation data at any desired propagation length.

as neutral density filters attached directly to the photodiode were adjusted at each test condition to guarantee that the analog signal did not go outside of the +/-5 V limit. Exceeding this limit would have saturated the sensor and resulted in a loss of sensitivity within the data.

In order to make the raw data from the photodetector useful for analysis the following procedure was used to scale the analog signal and then compute σ_χ^2. The 2-channel balanced photo diode outputs are defined in the following manner: scintillated fiber I, un-scintillated beam I_o, and linear amplified difference between the two channels $\Delta I = C(I - I_o)$.

$$I_{Normalized} = \frac{\Delta I - \langle \Delta I \rangle}{C} + \langle I \rangle \tag{6.14}$$

$$C = \langle \frac{\Delta I}{I - I_o} \rangle \tag{6.15}$$

$$\chi = \frac{1}{2} ln(\frac{I}{I_o}) = \frac{1}{2} ln(\frac{I_{Normalized}}{\langle I_o \rangle}) \tag{6.16}$$

$$\sigma_\chi^2 = \frac{\langle \chi^2 \rangle - \langle \chi \rangle^2}{\langle \chi \rangle^2}. \tag{6.17}$$

The 5 minutes of collection was broken up into 10 second intervals in order to mitigate slight signal drift in the sensor that was found to occur at long run times. The divisor C was computed

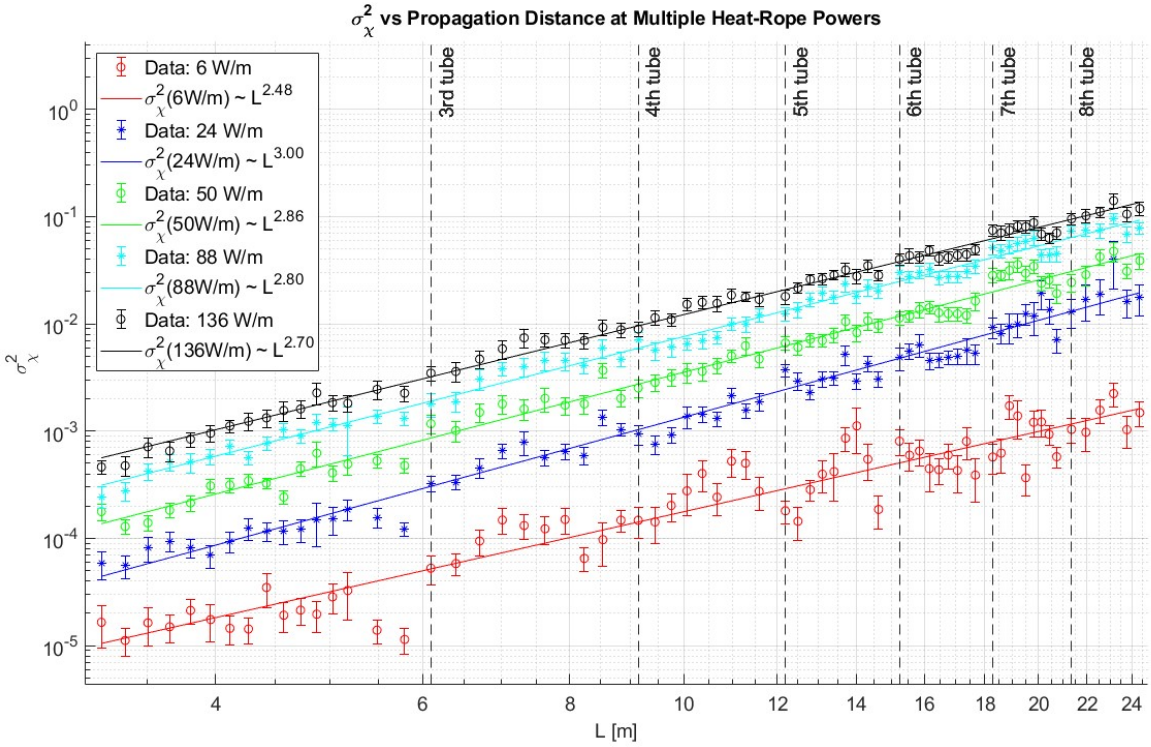

Figure 6.4: σ_χ^2 as a function of propagation distance and heat rope power within the SAF. Best fit lines are plotted with the exponential scaling factor listed in the legend. First 8 ft of collection is excluded due to the data being too close to the sensor noise floor.

and applied at each 10 second interval. An array of σ_χ^2 values was compiled containing a measurement at each 10 second interval. This array was then averaged to return the average σ_χ^2 for each propagation distance and heat rope power condition.

6.3 Results

The σ_χ^2 values within the SAF are plotted with respect to propagation distance and heat rope power in figure 6.4.

General trends can now be assessed and attributed to turbulence and optical parameters. Primarily, it can be seen by the scale of the fitted trend lines shown in the legend of figure 6.4 that $\sigma_\chi^2 \propto L^3$ throughout the SAF. This scaling is present regardless of the heat roper power applied. It can be concluded that the entirety of the SAF exists in the geometric optics regime. The beam intensity fluctuation's primary contributor is from refractive phenomenon and contributions from

diffraction can be considered negligible.

Furthermore, the effect of the increased heat rope power on scintillation can also be seen in figure 6.4. Referring to the scaling relationships derived in equation 2.10 for the geometric regime, scintillation is proportional to C_n^2 and inversely proportional to l_o. It was shown in the inner scale correlation experiment that l_o decreases and in the FRS experiment C_n^2 increases at higher heat rope powers. Figure 6.4 proves the model correct. As heat rope power is increased the proportionality of scintillation with respect to C_n^2 and l_o behaves as predicted.

It was explained in the background discussion that the size of the inner scale also has an effect on the distance it takes to transition to the diffractive or $L^{11/6}$ scaling regime. Since the wavelength of the laser is held constant, the largest Fresnel number should occur at the furthest distances and at the higher heat rope power due to their effects on the Fresnel number parameters (equation 2.14). Analyzing the furthest distances of the highest power case (136 W/m), it can be seen that the SAF is still scaling at L^3. No transition has occurred.

Validation of C_n^2 and l_o scaling can also be drawn from the temporal intensity data set. A hint at the magnitude of C_n^2 and the relative size of the turbulent length scales can be seen in the temporal spectrum of σ_χ^2. Figure 6.5 shows a temporal spectrum of an intensity data set at 2 propagation distances and varied heat rope settings. It can be seen that the total integrated power density of the intensity increases with heat rope power at constant propagation distance, L. This can be shown by reference to the spectral reproduction of σ_χ^2 in equations 6.21 and 6.20. If C_n^2 is assumed constant along the path, the increase in total power at all frequencies can be attributed to an increase in C_n^2.

Also notice that the higher power test cases contain higher frequency content. Higher frequency fluctuations in intensity correspond to smaller turbulent scales effecting the beam. This phenomenon can be validated by once again analyzing the spectral equations 6.21 and 6.20. When this spectrum is solved for various inner scale values, there is higher energy content within $\Phi_n(\kappa)$ at smaller values of l_o. Therefore, the higher frequency content in the index of refraction spectrum directly causes higher frequency content in the beam scintillation.

Analyzing the PDF of the log-amplitude intensity also gives insight into the mechanisms ef-

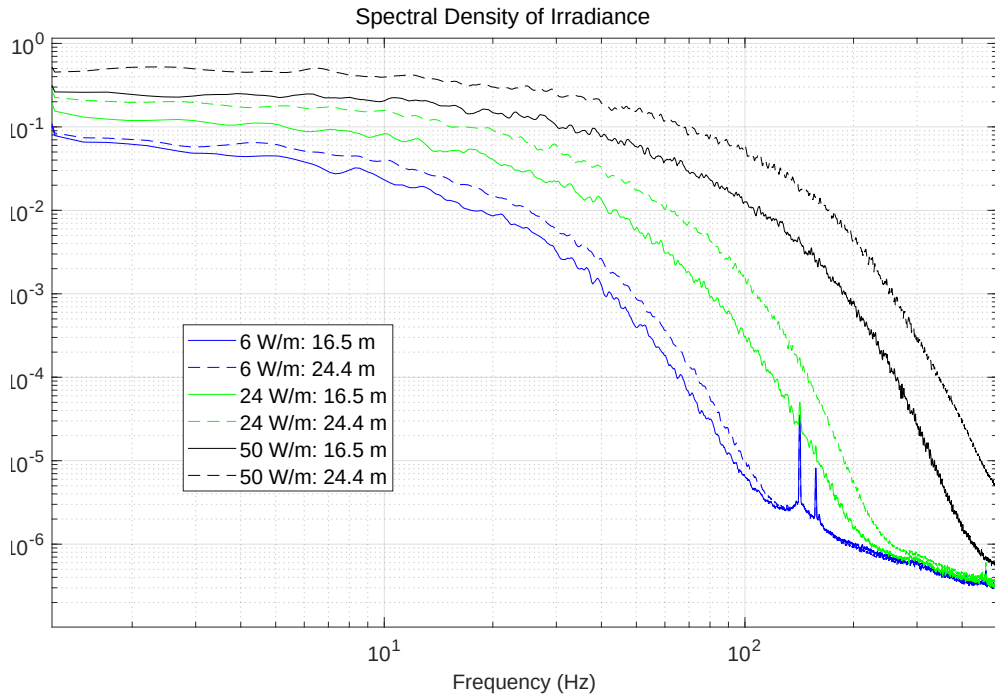

Figure 6.5: Power spectral density of beam intensity measurements at various SAF conditions. The spike in power in the 6 W/m case around $10^2 Hz$ is most likely due to the frequency of the overhead lights being captured in the data.

fecting the intensity fluctuation. Figure 6.6 shows the normalized PDF at various heat rope powers and heat rope distances. PDF a) in figure 6.6 is the highest scintillation value within the data set. Notice how this PDF is skewed to the lower intensity values as well as has the largest maximum value. The lower magnitude fluctuation cases shown in figure 6.6 c) and b) show a flatter PDF that denotes less content in the focused, high intensity, regimes.

Figure 6.7 shows K_3 as a function of propagation distance and heat rope power. This metric tells how closely a particular SAF condition can be recreated with the LN distribution. The larger heat rope powers and longer propagation distances result in a more skewed data set, denoting a divergence from log-normalcy.

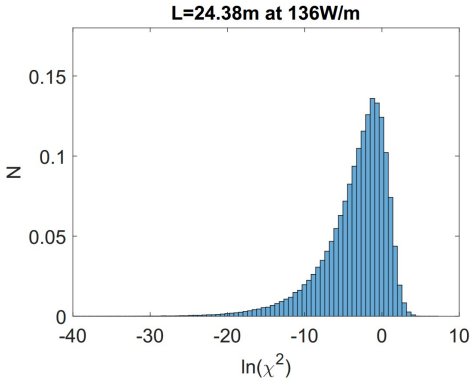

(a) maximum allowable distance L and 136 W/m heat rope power

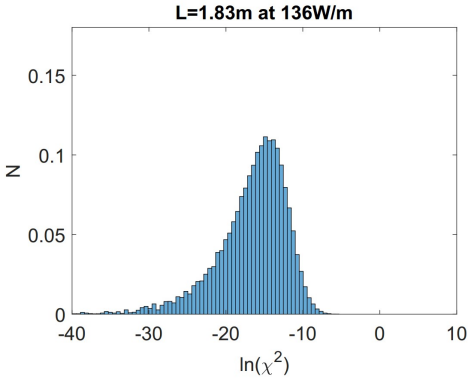

(b) 1.83 m of propagation distance at 136 W/m heat rope power

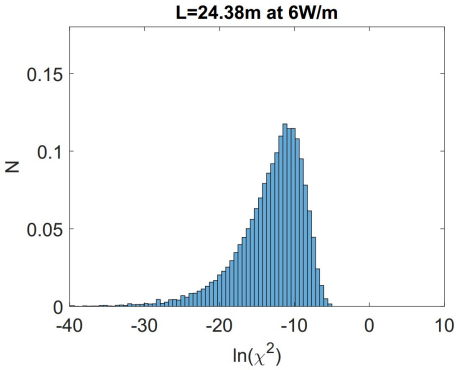

(c) maximum allowable distance L and 6 W/m heat rope power

Figure 6.6: Normalized probability distribution functions

6.4 Comprehensive Results

The results from each experiment have been laid out. Although, the main purpose of this study was to quantify the SAF in a comprehensive manner. Therefore, the experiment specific results described previously will now be compared in order to derive mathematical models as well as create scaling plots.

First off, the proof that the SAF exists in the geometric, refraction dominating, L^3 regime allows for the justification of approximations. Most AO effects within the SAF can be attributed to refraction, thus simplifying mathematical models by collapsing the diffractive contributions.

In singling out the vertical and horizontal gradients in refractive index by Schlieren imaging it

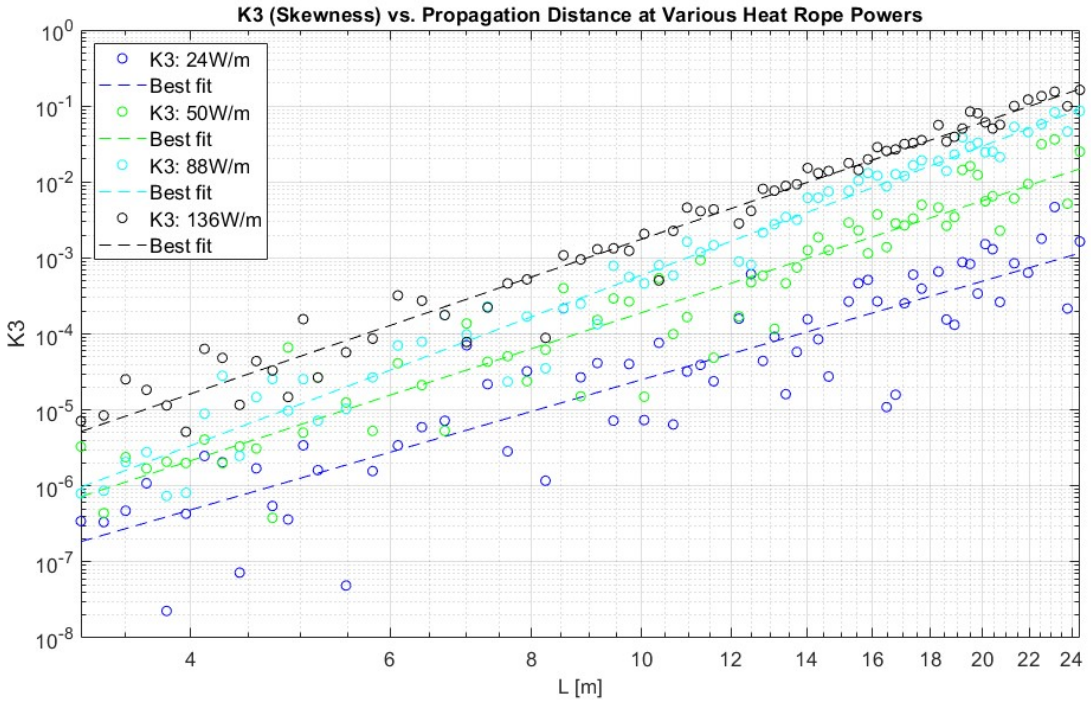

Figure 6.7: K3 cumulant at various heat rope powers as a function of distance. The larger K3 values depict a higher skew to the probability distribution function.

was proven that the cross section of the turbulent flow field is not homogeneous. Homogeneity is one of the primary assumptions when deriving the L^3 scaling law [5]. If the scintillation data set would have returned exactly L^3 scaling then the two experiments would have not been in agreement. Some error must be attributed to this non-homogeneity. The scintillation data followed this resolution by finding inconsistencies of scaling with respect to heat rope power. These inconsistencies provide insight into the commonly neglected fact that AO facilities might not follow an exact L^3 or $L^{11/6}$ scaling law. Simply assuming that the AO environment is ideal (in this case homogeneous) can lead to differences between actual and predicted conditions within the facility. It is difficult to create truly homogeneous turbulence. Therefore, most laboratory based AO facilities will contain some degree of asymmetry or directionality in the turbulent flow field. Understanding the effect this asymmetry has on the facility under investigation is imperative to a rigorous characterization, validation of engineering devices, and other AO research pursuits conducted in the facility.

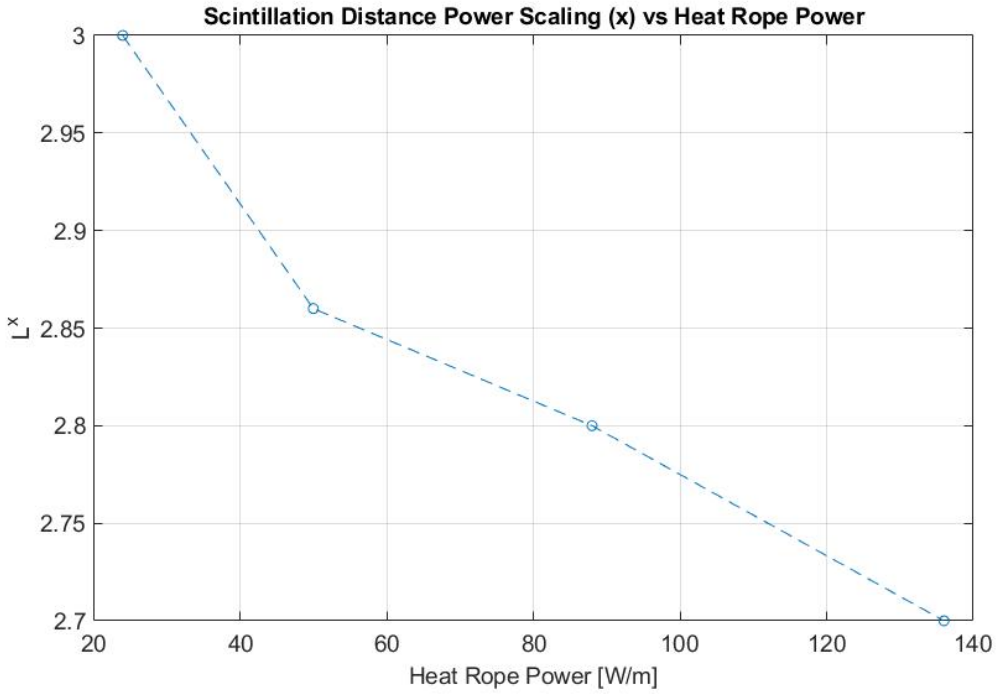

Figure 6.8: The dependence of heat rope power on the propagation distance power scaling.

For the SAF, referring to figure 6.8 will give a more comprehensive analysis than assuming all heat rope powers return exactly L^3 scaling. Figure 6.8 shows that the propagation distance scaling is inversely proportional to heat rope power. It should be noted that the lowest 6 W/m case was excluded from this graphic due to the high degree of error. While the scintillation at the 6 W/m case did increase with distance as expected, the spread of the data is too large to accept the returned distance scaling as an accurate representation of the facility. Using figure 6.8 one can now interpolate what the distance scaling might be for intermediate heat rope powers.

With the full set of characterization experiments completed the parallel beam correlation experiment is now revisited. It has been mentioned in chapter 4, that the inner length scale is the most influential to the beam scintillation in the geometric regime. In chapter 2 of Andrew's book over modeling optical scintillation it is shown that the most influential turbulent length scale varies with the intensity of the turbulent field [16]. In Andrew's proof, it is also revealed that on the onset of moderate to strong irradiance fluctuations the spatial coherence radius ρ_o begins

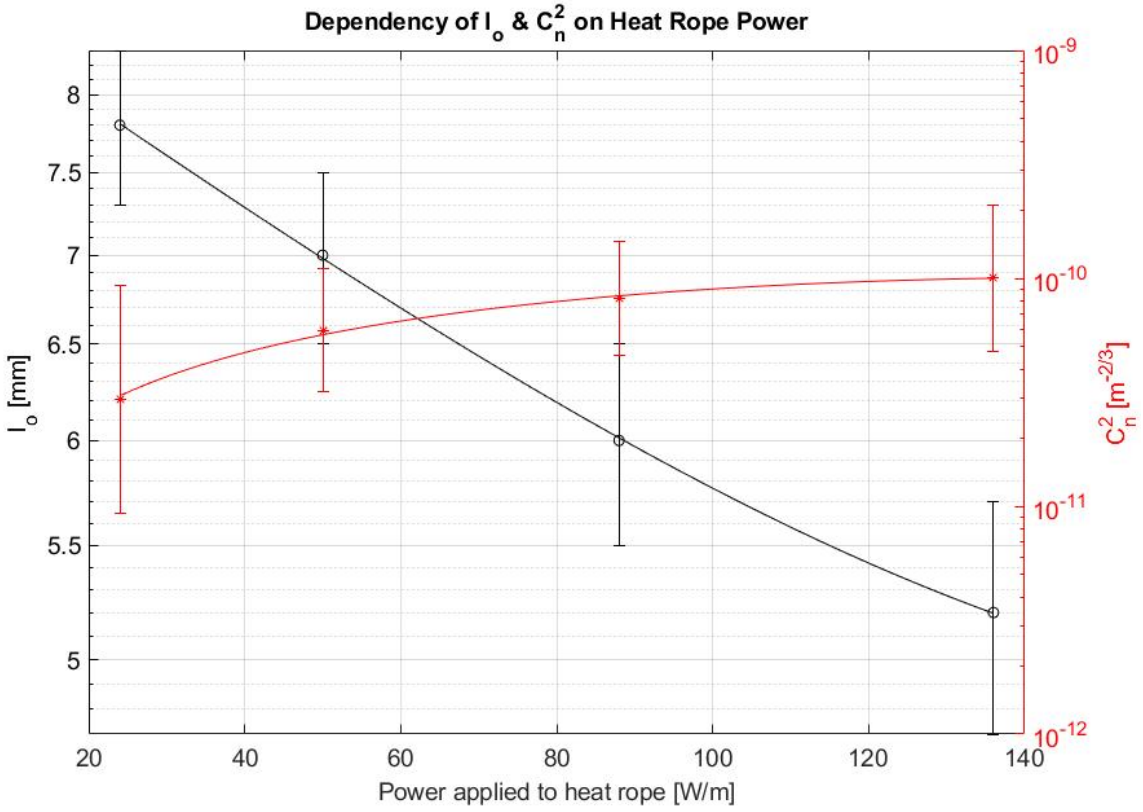

Figure 6.9: Decoupled C_n^2 and l_o dependence on heat rope power. C_n^2 is found using equation 5.21, a value of $C_n'^2 = 6.0$, and $\langle \rho'^2 \rangle$ from FRS. l_o was found using the methodology laid out in the parallel beam correlation experiment described in chapter 4.

to be a major contributor as well. With the C_n^2 values within the SAF being as high as they are ($C_n^2(136W/m) = 1.01 \times 10^{-10}$) in comparison to C_n^2 values within the actual atmosphere ($C_n^2(atm.) \approx 1 \times 10^{-15}$) the conditions within the SAF could be approaching moderate strength fluctuations. As a result, the most influential turbulent length scale could be in a transitional regime between the two parameters. In the explanation of the Consortini method for deriving l_o it was stated that the distance between beams, d, is assumed to be l_o [31]. This fact was made in conjunction with regime dependent assumptions. Although, the way the parallel beam experiment is framed insures that the scale extracted (d at maximum $B_y - B_x$) is in fact the most influential scale not just simply the inner scale. This is the advantage of using an optical experiment such as the one used in chapter 4 to derive turbulent length scales. Other methods such as CTA probes or

inner scale extraction from angle of arrival measurements [15] do not share this advantage. The parallel beam correlation experiment directly extracts the most influential scale. The coupling of the other experiments with the parallel beam correlation experiment validates the SAF characterization method. The non L^3 scaling and moderately high C_n^2 cause concern. This issue is resolved by conducting a turbulent scale experiment that does not rely on the inner scale assumption at all. The experiment instead inherently derives the most influential scale no matter the label.

The experiments have now been validated by each other, returning a facility wide characterization of the SAF. The figures 6.10 and 6.9 contain the results of the experiments comprehensively compiled in a way that intensity fluctuation and turbulent characteristics can be interpolated at every facility state.

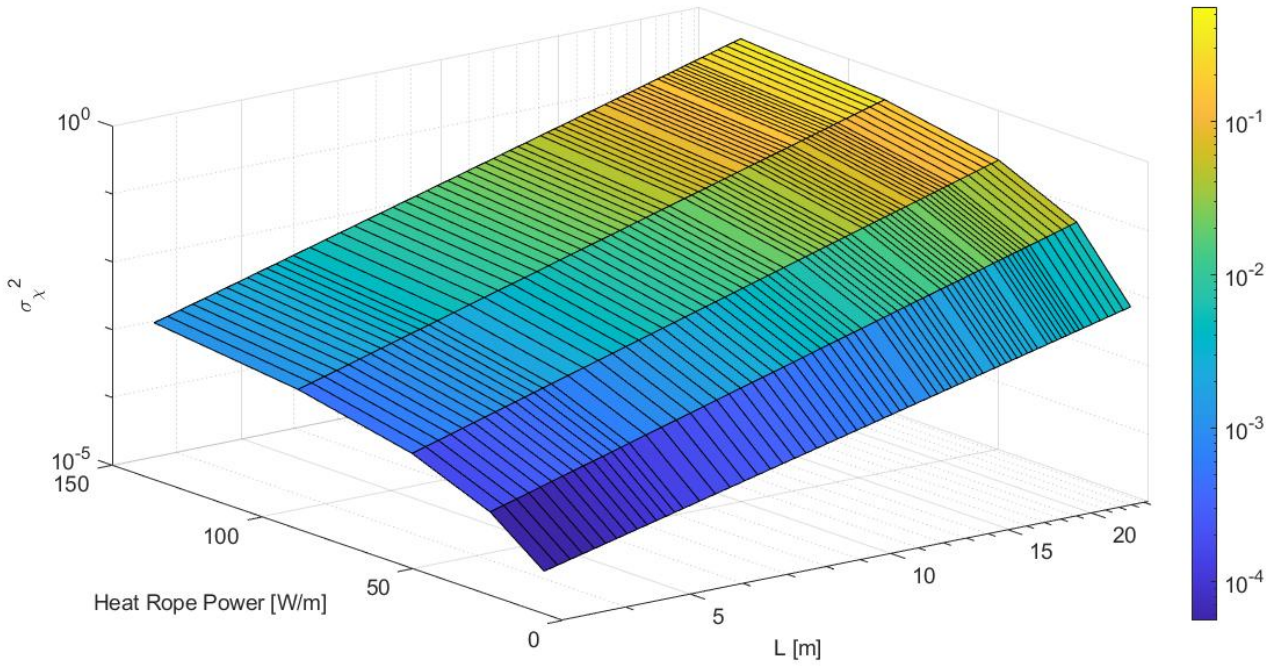

Figure 6.10: Surface plot of σ_χ^2 as a function of propagation distance L and heat rope power.

6.5 Comparison to Theory

Now that the parameters of the SAF have been defined with theoretical caution, as an exercise these findings will now be compared to commonly used theory for validation of results.

A simple explanation of the optical and turbulent parameters that had an effect on scintillation was described in chapter 2. This order of magnitude analysis was important for defining experimental plans, but is not refined enough to use for comparison of results. For a more comprehensive method of $\sigma_c hi^2$ estimation Tatarskii's spectral derivation will be used instead[5]. This derivation uses a power spectral density (PSD) of the refractive to define the intensity fluctuations or scintillation [44]. The PSD of the refractive index ,Φ_n, is found by computing the Fourier transform of the covariance between two points in the medium, B_n,

$$\Phi_n(\kappa) = \frac{1}{(2/pi)^3} \int d^3 r B_n(r) e^{-i\kappa r} \tag{6.18}$$

Kolmogorov's inertial subrange expression shown in 5.5 is now used to simplify $B_n(r)$ and the integral in equation 6.18 is transformed into spherical coordinates. $\Phi_n(\kappa)$ can then be expressed as proportional to C_n^2 and the limits of integration can be taken as l_o and L_o [1],

$$\Phi_n(\kappa) = \frac{5}{18\pi} C_n^2 \kappa^{-3} \int_{l_o}^{L_o} dr sin(\kappa r) r^{-1/3}. \tag{6.19}$$

In this analysis a modified Von Karman (MVK) PSD estimate shown in equation 6.20 was used [23].The MVK PSD estimates the spectral decomposition of the refractive index within the flow field using the same turbulence characteristics that were derived in the characterization experiments,

$$\Phi_n(\kappa) = 0.033 C_n^2 exp(\frac{-\kappa^2}{(5.92/l_o)^2(\kappa^2 + (2\pi/L_o)^2)^{11/6}}). \tag{6.20}$$

The modified Von Karman spectrum was chosen because it takes inner scale, outer scale, and refractive index fluctuation effects into account. The spectrum from equation 6.20 can be input into the plane-wave version of the scintillation dependence to find an estimate of σ_χ^2 for each

experimental condition [44].

$$\sigma_\chi^2 = \frac{1}{3}\pi^2 L^3 \int_0^\infty \Phi_n(\kappa)\kappa^5\, d\kappa, \quad L << l_o^2/\lambda \tag{6.21}$$

The laser wavelength defines $\kappa = 2\pi/\lambda$ and the experiments define values for l_o, C_n^2, and L_o. Equation 6.21 as a function of these quantities can now be plotted in congruence with the scintillation data to assess the agreement between experiment and theory.

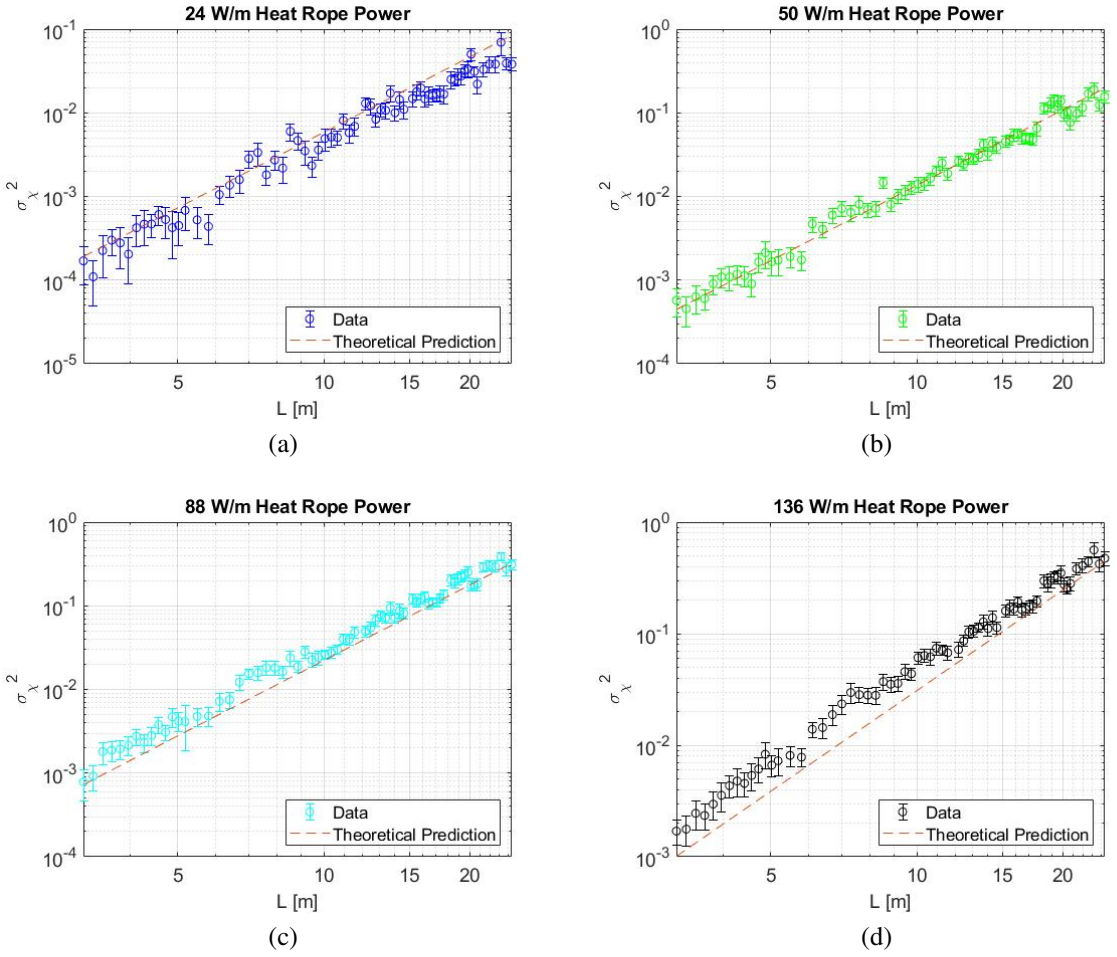

Figure 6.11: Comparison of scintillation data to a theoretical model for scintillation of a propagating plane wave. The model uses the modified Von Karman power spectrum in which the l_o and C_n^2 values from experiments were used as inputs.

The plots in figure 6.11 show that using the experimentally derived turbulence parameters for the inputs of equations 6.21 and 6.20 results in comparable values of scintillation to those found in the experiment. This shows that the experimentally found turbulence parameters are of the correct orders of magnitude and scale in the correct manner to heat rope power. Despite the fact that the turbulence within the SAF is not homogeneous, the theoretical model for scintillation is justified as an approximation for scintillation within the facility.

7. CONCLUSION AND FUTURE WORK

7.1 Future Work

The SAF has been operational since Summer of 2021. The experiments described herein are but the first of many to be conducted in this facility. As previously mentioned, the SAF is modifiable and controllable to meet the needs of many types of experiments. It was proposed that the primary experiments conducted in this new facility would be for the purpose of characterization. More complex experiments could then rely on the results of the characterization study for more knowledgeable preemptive design.

The final piece of characterization is a path dependent measurement of the wavefront aberration induced by the heat rope turbulence and scaled by propagation distance. Referring to Tatarskii [5], both intensity and phase fluctuations are brought about by turbulent interaction. The phase fluctuation follows different scaling laws as well as contains different dependencies on environmental parameters. Therefore, an experiment is being conducted within the SAF to characterize wavefront fluctuation as a function of propagation distance and heat rope power. The similarity in testing conditions to that of the scintillation experiment will allow for a one to one comparison of data as well as the possibility of novel ways to extract AO parameters of interest from the comparison of the intensity and wavefront data sets.

Furthermore, the SAF is a predecessor to a larger AO facility under construction at Texas AM's RELLIS campus. This facility is referred to as the Ballistic, Aero-Optics, and Material (BAM) test range. The Aero-Optic portion of BAM will consist of a 1 km long climate controlled tunnel that will house heat ropes similar to those within the SAF. This facility will have the capability to test more powerful laser systems at further propagation distances than the SAF. The BAM will need to be rigorously characterized to the same degree that the SAF was. The procedure laid out in this study was created with the future need to characterize BAM in mind. As a result, the characterization method herein will be used for that facility as well.

7.2 Conclusion

In this study a set of experiments were designed and conducted to characterize a newly constructed atmospheric optic facility. The facility under investigation was the Subscale Atmospheric Facility (SAF). This facility was shown to be a platform in which a multitude of controlled and reproducible tests could be carried out. Prior to more complex experimentation, the SAF's inherent parameters needed to be characterized. With the facility characteristics and dependencies defined, future testing campaigns within the SAF could leverage the parameter mapping to direct experimental plans.

The study began by imaging the turbulence created within the SAF via Schlieren imaging. It was found that the turbulent plume created by the heat rope was asymmetrical in the cross sectional plane of the tube. Furthermore, the Schlieren imaging showed that the turbulence became more erratic, contained finer structure, and increased refractive index gradients as the turbulence producing heat rope's power was increased. The qualitative knowledge of the turbulent plume structure helped refine the experimental procedure for subsequent tests.

In order to return an estimate of the influential turbulent length scale within the SAF, a non-obstructing parallel beam correlation experiment was presented. This experiment decoupled the turbulent length scale and turbulent strength (C_n^2) from one another by leveraging the phenomenon of beam jitter. The jitter between the 2 co-propagated beams was correlated in the in plane and out of plane directions. The distance between the 2 beams that resulted in the greatest difference between the 2 directional correlations was found. This distance was presumed to be an estimate of the most influential turbulent length scale, or inner length scale in the geometric regime case. It was found that the SAF contained inner length scales varying from 5.2 mm to 7.8 mm inversely proportional to the heat rope power applied.

The next experiment used a novel Filtered Rayleigh Scattering approach to finding the refractive index structure constant C_n^2. Using this non-obstructing laser light scattering method, a temporal and spatial measurement of the 2D variable density field created by the turbulent plume was found. Although, due to experimental difficulties, C_n^2 had to be calculated via a statistical

approach by utilizing the average RMS of density, $\langle \rho'^2 \rangle$. This experiment returned values of C_n^2 ranging from 2.93×10^{-11} to 1.01×10^{-10} $m^{-2/3}$ proportional to heat rope power applied.

The final characterization test was a full facility parameter sweep of laser beam intensity fluctuation or scintillation. The scintillation of a large diameter laser beam propagated through the center of the SAF was measured at various heat rope settings as well as propagation distances. The results concluded that the SAF scaled scintillation with propagation distance at approximately a value proportional to L^3 ($L^{2.48} - L^{3.00}$, dependent on heat rope power). This scaling law agrees with the theoretical prediction that the laser intensity fluctuation is dominated by refractive effects in the near field. The returned scaling value concluded that length of the SAF is not large enough for diffraction to have contributed to intensity fluctuations. The scintillation data set was then used as the link for other AO parameter validations due to the many dependencies inherent to the scintillation metric.

The experiments concluded in a facility characterization with respect to turbulence intensity and propagation distance. The methodology proposed was intentionally designed to minimize theoretical presumptions at each stage of testing. As a proof of theory and validation of experiments, the experimentally derived AO parameters were input into theoretical estimates of scintillation. It was found that the results of the scintillation experiment showed similarity to predicted values derived from theoretical models relying on inputs from the turbulence characterization experiments. Therefore, it can be concluded that the experiments herein are an adequate guide for the characterization of AO facilities similar to that of the SAF.

REFERENCES

[1] R. K. Tyson, *Principles of Adaptive Optics, Third Edition*. CRC Press, 2011.

[2] A. J. MacGovern, D. A. Nahrstedt, and M. M. Johnson, "Atmospheric propagation for tactical directed energy applications," *Proceedings of SPIE*, 2000.

[3] W. O. Popoola, Z. Ghassemlooy, C. G. Lee, and A. C. Boucouvalas, "Scintillation effect on intensity modulated laser communication systems—a laboratory demonstration," *Optics Laser Technology*, 2010.

[4] T. V. Karman, "The fundamentals of the statistical theory of turbulence," *Journal of the Aeronautical Sciences*, 1937.

[5] V. Tatarskii, "The effects of the turbulent atmosphere on wave propagation," *Isreal Program for Scientific Translations*, 1971.

[6] H. T. Yura and S. G. Hanson, "Optical beam wave propagation through complex optical systems," *JOSA*, 1987.

[7] R. B. Holmes, V. S. R. Gudimetla, J. Lucas, and J. F. Riker, "Scintillation of light from distant objects due to anisotropic and non-kolmogorov turbulence," *AMOS*, 2013.

[8] L. C. Andrews, R. L. Phillips, R. Crabbs, and T. Leclerc, "Deep turbulence propagation of a gaussian-beam wave in anisotropic non-kolmogorov turbulence," in *Laser Communication and Propagation through the Atmosphere and Oceans II*, 2013.

[9] E. S. Manulovich, V. A. Astapenko, and P. A. Golovinskii, "Propagation of ultrashort laser pulses in dry and humid air," *Atmos Ocean Opt*, 2015.

[10] K. Kumari and D. A. Donzis, "Regimes of optical propagation through realistic turbulence: theory and direct numerical simulations," *Waves in Random Complex Media (under review)*, 2022.

[11] E. J. Jumper and S. Gordeyev, "Physics and measurement of aero-optical effects: Past and present," *Annual Review Fluid Mechanics*, 2017.

[12] C. I. Moorea, H. R. Burrisb, W. S. Rabinovichc, L. Wasiczkoa, M. R. Suitea, L. A. Swingenc, R. Mahond, M. F. Stellb, G. C. Gilbreathe, and W. J. Scharpt, "Overview of nrl's maritime laser communication test facility," *Proceedings of SPIE*, 2005.

[13] R. Q. Fugate, B. L. Ellerbroek, E. J. Stewart, D. Colucci, R. E. Ruane, J. M. Spinhirne, R. A. Cleis, and R. Eager, "First observations with the starfire optical range 3.5-meter telescope," *Proc. SPIE*, 1994.

[14] R. Mahon, C. I. Moore, H. R. Burris, M. Ferraro, W. S. Rabinovich, M. Suite, and L. M. Thomas, "Probability density of irradiance fluctuations observed over terrestrial ranges," *Applied Optics*, 2011.

[15] A. Consortini, Y. Y. Sun, C. Innocenti, and Z. P. Li, "Measuring inner scale atmospheric turbulence by angle of arrival and scintillaion," *Optics Communication*, 2003.

[16] L. C. Andrews, R. L. Phillips, and C. Y. Young, *Laser Beam Scintillation with Applications*. SPIE, 2001.

[17] F. S. Veterlino, C. Young, L. Andrews, K. Grant, K. Corbett, and B. Clare, "Scintillation: theory vs. experiment," *Proceedings of SPIE*, 2005.

[18] M. B. Roopashree, A. Vyas, S. A. Krishnan, R. S. Ram, S. S. Sai, and B. R. Prasad, "Towards low cost turbulence generator for aotesting: Utility, control and stability," *Imaging and Applied Optics Technical Digest*, 2011.

[19] A. K. Majumdar and H. Gamo, "Statistical measurements of irradiance fluctuations of a multipass laser beam propagated through laboratory-simulated atmospheric turbulence," *Applied Optics*, 1982.

[20] R. A. Elliot, J. R. Kerr, and P. A. Pincus, "Optical propagation in laboratory-generated turbulence," *Applied Optics*, 1979.

[21] G. DiComo, M. Helle, J. Penano, A. Ting, A. Schmitt-Sody, and J. Elle, "Implementation of a long range, distributed-volume, continuously variable turbulence generator," *Applied Optics*, 2016.

[22] R. J. Watkins, K. Dai, G. White, W. Li, J. K. Miller, K. S. Morgan, and E. Johnson, "Experimental probing of turbulence using a continuous spectrum of asymmetric oam beams," *Optics Express*, 2020.

[23] J. D. Schmidt, *Numerical Simulation of Optical Wave PropagationWith examples in MATLAB*. SPIE, 2010.

[24] J. Strohbehn, *Laser Beam Propagation in the Atmosphere*, ch. Modern theories in the propagation of optical waves in a turbulent medium", pp. 45–106. Springer Berlin Heidelberg, 1978.

[25] S. Rasouli and M. T. Tavassoly, "Measurement of the refractive-index structure constant, c_n^2, and its profile in the ground level atmosphere by moire technique," *Proceedings of SPIE*, 2006.

[26] S. F. Clifford, G. R. Ochs, and R. S. Lawrence, "Saturation of optical scintillation by strong turbulence," *JOSA*, 1973.

[27] T. P. Davis, "Schlieren photography - short bibliography and review," *Optics and Laser Technology*, 1981.

[28] W. C. Gardner, Y. Hidaka, and T. Tanzawa, "Refractivity of combustion gases," *Flame 40, 213*, 1981.

[29] G. S. Settles, *Schlieren und shadowgraph techniques: visualizing phenomena in transparent media*. Springer, 2001.

[30] R. A. Meyers, "Atmospheric turbulence," in *Encyclopedia of Physical Science and Technology (Third Edition)*, Academic Press, 2003.

[31] A. Consortini and K. A. O'Donnell, "Measuring the inner scale of atmospheric turbulence by correlation of lateral displacements of thin parallel laser beams," *Waves in Random Media*, 1993.

[32] K. L. Baker and M. M. Moallem, "Iteratively weighted centroiding for shackhartmann wave-front sensors," *Optics Express*, 2007.

[33] D. G. Perez and G. Funes, "Beam wandering statistics of twin thinlaser beam propagation undergeneralized atmospheric conditions," *Optics Express*, 2012.

[34] S. Nowlin, I. Hahn, R. Hugo, and K. Bishop, "Concurrent aerial and groundbased optical turbulence measurements along along, elevated path," *Proceedings of SPIE*, 1999.

[35] R. P. Feynman, *The Feynman Lectures on Physics*, ch. The Origin of the Refractive Index. Assison-Wesley Pub. Co., 1963.

[36] S. Gang, W. Ning-Quan, X. Li-Ming, and W. Yi, "Profile and character of atmospheric structureconstant of refractive index c_n^2," *Atmospheric and Oceanic Science Letters*, 2015.

[37] P. Moin, "Revisiting taylor's hypothesis," *Journal of Fluid Mechanics*, 2009.

[38] R. B. Miles, W. R. Lempert, and J. N. Forkey, "Laser rayleigh scattering," *Meas. Sci. Technol.*, 2001.

[39] C. M. Penney, "Light scattering in terms of oscillator strengths and refractive indicies," *JOSA*, 1969.

[40] G. S. Elliot, N. Glumac, C. D. Carter, and A. S. Nejad, "Two-dimensional temperature field measurements using a molecular filter based technique," *Combustion Science and Technology*, 2007.

[41] J. N. Forkey, W. R. Lempert, and R. B. Miles, "Corrected and calibrated i2 absorption model at frequency doubled nd:yag laser wavelengths," *Appl. Opt.*, 1997.

[42] X. Pan, M. N. Shneider, and R. B. Miles, "Coherent rayleigh-brillouin scattering in molecular gases," *Phys. Rev. A*, 2004.

[43] C. M. Limbach, *Characterization of Nanosecond, Femtosecond and Deal Pulse Laser Energy Depostion in Air for Flow Control and Diagnostic Applications*. PhD thesis, Princeton University, 2015.

[44] R. S. Lawerence and J. W. Strohbehn, "A survey of clear-air propagation effects relevant to optical communications," *IEEE*, 1970.

[45] K. Kiyono, "Log-amplitude statistics of intermittent and non-gaussian time series," *Physical Review E*, 2009.

[46] A. D. Wheelon, "Skewed distribution of irradiance predicted by the second-order rytov approximation," *JOSA*, 2001.

[47] D. L. Fried, "Aperture averaging of scintillation," *JOSA*, 1967.

[48] J. H. Churnside, "Aperture averaging of optical scintillations in the turbulent environment," *Appl. Opt.*, 1991.